Science
AAAS

Supplementary Materials for

Sound induces analgesia through corticothalamic circuits

Wenjie Zhou *et al*.

Corresponding authors: Yuanyuan Liu, yuanyuan.liu@nih.gov; Wenjuan Tao, wjtao01@ahmu.edu.cn; Zhi Zhang, zhizhang@ustc.edu.cn

Science **377**, 198 (2022)
DOI: 10.1126/science.abn4663

The PDF file includes:

Other Supplementary Material for this manuscript includes the following:

Materials and Methods

Animals

In this study, 8–10 weeks old male and female C57BL/6J and *CaMKII-Cre* mice (purchased from Charles River or Jackson Laboratories) were used. These mice were housed, 3–5 per cage in a colony, in a stable environment (23–25 ℃ ambient temperature) with *ad libitum* access to standard lab mouse pellet food and water on a 12 h light/12 h dark cycle (lights on from 07:00 to 19:00). Mice were randomly assigned into different groups and all experiments were conducted with the approval of the Animal Care Committee of the University of Science and Technology of China (USTC).

Complete Freund's adjuvant and capsaicin injection

Inflammatory pain was induced by injecting complete Freund's adjuvant (CFA,10 μL, Sigma) into the plantar surface of the left hindpaw or forepaw of each mouse under brief isoflurane anesthesia. To induce persistent inflammatory pain, a second injection of the CFA was administered 10 days after the first injection.

Capsaicin (Sigma) dissolved in saline containing 10% ethanol and 10% Tween-80 was injected intradermally into the left hindpaw (100 μg/ml, 10 μl) to induce tonic pain.

Control mice received an intradermal injection of the same quantity of saline (0.9% NaCl) or vehicle.

Neuropathic pain

All SNI surgeries were performed under isoflurane (3% for induction/2% for maintenance) anesthesia. In brief, the skin of the left thigh was incised, and the muscle was gently separated to expose the sciatic nerve bundle, which is composed of the sural, common peroneal, and tibial nerves. After exposure of these nerves, the common peroneal and tibial nerves were tightly ligated by using nonabsorbent 4-0 chromic gut and transected distally, while the sural nerve was left intact. Finally, the skin was sutured and disinfected with iodophor. A similar procedure was performed for sham mice without causing any nerve damage.

Stereotaxic surgery and virus injection

Mice were deeply anesthetized using isoflurane with oxygen (3% for induction; 1.5–2% for maintenance) and mounted on a stereotaxic frame (RWD, Shenzhen, China). The body temperature of these mice was maintained at 36 ℃ using a heating pad. A small craniotomy above the target brain region was performed using a dental drill, and the skull was

carefully removed. The eyes of the mice were kept moist using ophthalmic ointment throughout the surgery. Virus was infused into the target areas using a fine glass micropipette with a tip diameter of 10–15 μm, which was connected to a 10-μL syringe (Hamilton, USA). The speed and volume of the injection were controlled using a micro-infusion pump (micro 4, WPI). The pipette was left in the place for an additional 5 min after the end of the injection and then withdrawn slowly to avoid back-flow of virus.

For anterograde tracing, rAAV-hSyn-DIO-mGFP-T2A-Synaptophysin-mRuby-WPRE-hGH pA (AAV-DIO-mGFP-Synaptophysin-mRuby, 4.7×10^{12} viral genome (vg) ml^{-1}, 200 nl, BrainVTA) was injected into the ACx (AP, −2.40 and −2.65 mm; ML, −4.90 mm with a 10° angle; DV, −0.80 mm) or the MGB (AP, −2.70 mm; ML, −2.40 mm; DV, −3.25 mm) of *CaMKII-Cre* mice. To visualize the PO and VP neurons innervated by the ACx, the anterograde trans-synaptic virus AAV2/1-hSyn-Cre-WPRE-pA (AAV1-Cre, 2.1×10^{13} vg mL^{-1}, 180 nl for each site, Taitool) was injected into the ACx, and the Cre-dependent AAV2/9-hEF1a-DIO-EGFP-WPRE-pA (AAV-DIO-EGFP, 2.0×10^{12} vg mL^{-1}, 250 nl, BrainVTA) was injected into the ipsilateral PO (AP, −2.40 mm; ML, −1.28 mm; DV, −3.20 mm) or VP (AP, −2.25 mm; ML, −1.78 mm; DV, −3.35 mm). Then, the scalp was sutured, and the mice were returned to their home cages to allow for viral expression. Three weeks later, the mice were deeply anesthetized and transcardially perfused, and the brains were cryosectioned for examining the mRuby signals originating from ACx^{Glu} neurons or MGB^{Glu} neurons in the whole brain or the EGFP fluorescence signals in the PO and VP.

For retrograde tracing, AAV2/2Retro-hSyn-eGFP-WPRE-pA (rAAV2/2-EGFP, 6.84×10^{12} vg mL^{-1}, 180 nl, Taitool) and AAV2/2Retro-hSyn-tdTomato-WPRE-pA (rAAV2/2-tdTomato, 1.51×10^{13} vg mL^{-1}, 180 nl, Taitool), which could be absorbed by the terminals at the injection site and transported retrogradely to the soma to express the EGFP or tdTomato, were injected into the PO or the VP. After 3 weeks, the mice were killed, and brain slices were stained with an antibody against GABA or an antibody against glutamate in the ACx.

For optogenetic activation of the ACx^{Glu}→PO, ACx^{Glu}→VP or ACx^{Glu}→ICx circuits, the Cre-dependent virus AAV-DIO-ChR2-mCherry (250 nl for each site) was micro-infused into the ACx of *CaMKII-Cre* mice. For optogenetic inhibition of the ACx^{Glu}→PO, ACx^{Glu}→VP or ACx^{Glu}→ICx circuits, the Cre-dependent virus AAV2/9-EF1α-DIO-eNpHR3.0-EYFP-WPRE-hGH polyA (AAV-DIO-eNpHR3.0-EYFP, 1.3×10^{13} vg mL^{-1}, 250 nl for each site, BrainVTA) was delivered into the ACx of *CaMKII-Cre* mice. Meanwhile, an optical fiber was implanted towards the PO, the VP or the IC (AP, −0.35mm; ML, −5.50 mm with a 15° angle; DV, −0.20 mm), and then secured to the skull using dental cement. For selective chemogenetic activation or inhibition of PO and VP neurons innervated by the ACx, the anterograde trans-synaptic virus AAV1-Cre was delivered into the ACx, and Cre-dependent AAV2/9-

EF1α-DIO-hM3D(Gq)-mCherry-WPREs (AAV-DIO-hM3Dq-mCherry, 5.54 × 10^{12} vg mL^{-1}, 200 nl, BrainVTA) or rAAV-EF1α-DIO-hM4D(Gi)-mCherry-WPREs (AAV-DIO-hM4Di-mCherry, 2.86 × 10^{12} vg mL^{-1}, 200 nl, BrainVTA) was injected into the ipsilateral PO or VP. The mice injected with the Cre-dependent AAV2/9-EF1α-DIO-EYFP-WPRE-hGH polyA (AAV-DIO-EYFP, 3.42 × 10^{12} vg mL^{-1}, 200 nl, Brain Case) or AAV2/9-EF1α-DIO-mCherry-WPRE-hGH polyA (AAV-DIO-mCherry, 6.76 × 10^{12} vg mL^{-1}, 200 nl, Brain Case) virus at the same volume were used as controls.

For *in vivo* single-cell Ca^{2+} imaging of VP- and PO-projecting ACx neurons in freely moving mice, retroAAV2/2-Cre (9.55 × 10^{12} vg mL^{-1}, 200 nl, Brain Case) virus, which could be absorbed at the terminals at the injection site and retrogradely transported back to the soma to express the Cre enzyme, was injected into the PO or the VP. The Cre-dependent AAV-DIO-GCaMP6m (1.0 × 10^{13} vg mL^{-1}, 200 nl, Brain Case) virus was also injected into the ipsilateral ACx. For *in vivo* Ca^{2+} imaging of the PO and VP neurons receiving ACx projections at single-cell resolution, the anterograde trans-synaptic AAV1-Cre virus was delivered to the ACx, and Cre-dependent AAV-DIO-GCaMP6m was injected into the ipsilateral PO or VP. Three weeks later, the mice were anesthetized with isoflurane and fixed on a stereotaxic frame, and the scalp was removed. The skull above the target areas was carefully removed using high-speed dental drilling, and an integrated microendoscopic GRIN lens (0.5 mm in diameter × 6 mm in length, Inscopix, #1050-002211) was slowly lowered (100 μm/min) toward the target areas using a stable stereotaxic holder attachment. The GRIN lens was connected to a data acquisition system for online monitoring of calcium signals. Once the GCaMP6m-expressing neurons were detected, the GRIN lens was secured to the mice's skull with dental cement and the lens was capped for protection.

***In vivo* multi-tetrode recordings**

Mice were prepared for surgery as described above. For chronic extracellular recordings, a custom-built eight movable tetrode array was implanted into areas of interest, including the right VP, the PO, and the ACx. Each tetrode was made of four twisted platinum/iridium wires (12.5-μm diameter, California Fine Wire, Grover Beach, CA). A screw-based microdrive scaffold housing the electrodes was firmly mounted onto the skull with the dental cement. The mice were raised alone and allowed to recover for at least 3 days before recording, and the electrodes were lowered in steps of 70 μm for recording different neuronal ensembles. To verify the recording sites, the electrodes were coated with DiI dye before implantation. For electrophysiology combined with optogenetics, an optrode was constructed by surrounding an optical fiber with tetrode wires, and the tip of the optical fiber was about 200 μm above the tetrode tips. Recording electrodes were attached to a 32-channel headstage, and neuronal signals were amplified and stored

using a Neurostudio amplifier and Neurostudio data acquisition software (Greathink Medical Technology), and the raw data were filtered offline at a bandwidth of 300–5,000 Hz to obtain spike information. Spike sorting was performed with a sorting method involving the T-Dis E-M algorithm built in Offline Sorter 4 (Plexon, USA). The firing rates of sorted units were calculated using Neuroexplorer 5 (Nex Technologies, USA). Peristimulus histograms of firing rates were computed over a bin width of 5 ms for each unit between −0.2 and 0.8 s.

Optogenetic and chemogenetic manipulation

Before behavioral experiments, the mice were routinely handled by experimenters for 3 days. On the experiment day, the mice were transported to a testing room and were habituated for approximately 4 h. Then, the mice were anesthetized with isoflurane for connecting the chronically implanted fibers (diameter, 200 μm, Newdoon) to a laser generator using optic fiber sleeves, and then, the mice were returned to the home cage for at least 30 min. Next, blue light (473 nm, 5–8 mW, 15-ms pulses, 20 Hz) or yellow light (594 nm, 5–8 mW, constant), controlled by a Master-8 pulse stimulator (A.M.P.I.), was delivered to selectively activate or inhibit the ACx^{Glu} terminals in the PO and the VP. For chemogenetic manipulation, the chemical ligand CNO (5 mg/kg, Sigma) was intraperitoneally injected in these mice under isoflurane anesthesia. Behavior tests were then carried out at least 30 min later. The same stimulus protocols were applied to control animals. After the completion of all behavioral tests, the mice were killed for verifying the virus injection site and the optical fiber site. The data obtained from mice with missed target brain regions were excluded from our analysis. The brain slice schematics indicating the virus injection sites and optical fiber placement sites were modeled after the corresponding sections in Paxino's brain atlas were highlighted using Adobe Illustrator.

Auditory stimuli

The noise level of the environment was measured in decibels (dB) using a Sound Level Meter (AWA-5661-A, Aihua, Hangzhou). Auditory stimuli were generated in Adobe Audition 3.2 or a computer-controlled Auditory Workstation from Tucker-Davis Technologies (TDT, Alachua, FL) and delivered through an open-field magnetic speaker (MF1, TDT). SPL was calibrated using a condenser microphone (Center Technology, Taiwan). The consonant sound and dissonant sound are provided at https://ln5.sync.com/dl/ce0bb77d0/gr7bf4kf-hpfny94e-arsb3cy7-fehhgnis as previously used (*39*).

***In vivo* fiber photometry recordings**

Calcium signals were recorded by using fiber photometry. Briefly, a microinjection of an AAV-CaMKIIα-GCaMP6m (rAAV-EF1α-DIO-GCaMP6m-WPRE-hGH-pA, AAV2/9, 5×10^{12} vg/mL, 200 nl) virus and the implantation of an

optical fiber (200 μm OD, 0.37 NA, Inper) were carried out at the VP and PO, and the mice were allowed to recover for at least 2 weeks before recording. A mono fiber optic patch cord (Inper, MFO-1x2-F-W1.25-200-0.37-100) connected to the fiber photometry system (Inper) was attached to the implanted fiber optic cannula using a ceramic sleeve with black heat-shrinkable tubes. To record fluorescence signals from GCaMP6m, light from a 470-nm LED was bandpass filtered (470/10 nm), collimated, reflected by dichroic mirrors, focused using a 20× objective, and then delivered at a power of 25–40 μW at the tip of the fiber optic cannula. The emitted fluorescence from GCaMP6m was bandpass filtered (525/40 nm) and focused on the sensor of a CMOS camera. The end of the fiber was imaged at a frame rate of 60 fps with InperSignal, and the mean value of the ROI at the end-face of the fiber was calculated using InperPlot software. To serve as an isosbestic control channel, 410-nm LED light was bandpass filtered (410/10 nm) and delivered alternately with 470-nm LED light. GCaMP6m fluorescence intensity was then recorded before and during punctate mechanical stimuli (von Frey filaments). The values of fluorescence change (ΔF/F) were derived by calculating ΔF/F0 = F(t) − F0(t)/F0(t), and the signals at 5 s before stimulus presentation were defined as the baseline. All heatmaps and averaged Ca^{2+} traces with shaded areas denoting the standard error of mean were generated in InperPlot software (Inper Technology, Hangzhou).

Microendoscope imaging and data processing

Before data acquisition, a dummy scope (weight: 2 g) was attached to the baseplate, and the mice were habituated in the testing room for at least 2 days. On the day of Ca^{2+} imaging, the mice were head-attached to a microscope (Inscopic, USA), placed into a rectangular chamber, and then allowed to move freely. Noise was delivered via a speaker placed close to the chamber, and the sound intensity was measured in decibels (dB) using a Sound Level Meter. After habituation for at least 30 min, Ca^{2+} images were obtained using Vista acquisition software (Inscopix; LED power: 0.6–1.0 mW) at 20 Hz with a gain of 4.5. During the acquisition, images were recorded for 5 min without sound stimulation and were utilized as a baseline, and then, white noise of different intensities was delivered for 15 min.

The raw Ca^{2+} data were preprocessed by Mosaic (Inscopix) and custom-written scripts in MATLAB as previously described (*40*). In brief, the imaging data were 2× temporally down-sampled, and motion was corrected using default settings in the software. Then, fluorescence signals were normalized by their time-averaged mean (ΔF/F calculation), and the signals of putative individual cells were identified using standard principal components analysis (PCA)/independent components analysis (ICA) defaults in the software. Finally, sorted putative cells were manually chosen based on the locality of source pixels and asymmetric calcium transients in the resulting traces.

***In vitro* electrophysiological recordings**

For acute brain slices preparation, the mice were deeply anesthetized with pentobarbital sodium (2% w/v, i.p.) and subsequently intracardially perfused with ~20 mL of ice-cold oxygenated cutting solution that contained 93 mM N-methyl-d-glucamine (NMDG), 1.2 mM NaH_2PO_4, 2.5 mM KCl, 20 mM HEPES, 30 mM $NaHCO_3$, 2 mM thiourea, 25 mM glucose, 3 mM Na-pyruvate, 5 mM Na-ascorbate, 10 mM $MgSO_4$, 0.5 $CaCl_2$, and 3 mM glutathione (GSH). Then, the mice were quickly decapitated, and the brain was carefully removed from the skull. The brain was glued on the bed plate of a vibratome, and coronal slices (280 μm) that contained the PO or the VP were cut in ice-cold cutting solution sectioned at 0.18 mm s^{-1} (VT1200s, Leica). Then, these slices were initially incubated in cutting solution at 33 ℃ for 10–12 min and subsequently transferred into N-2-hydroxyethylpiperazine-N-2-ethanesulfonic acid (HEPES) artificial cerebrospinal fluid (ACSF) that contained 2.5 mM KCl, 92 mM NaCl, 30 mM $NaHCO_3$, 20 mM HEPES, 1.2 mM NaH_2PO_4, 2 mM thiourea, 25 mM glucose, 3 mM Na-pyruvate, 5 mM Na-ascorbate, 2 mM $MgSO_4$, 2 mM $CaCl_2$, and 3 mM GSH at 25 ℃ for at least 1 h. After incubation, the slices were placed in a recording chamber (Warner Instruments, USA) for electrophysiological recording and were continuously perfused with oxygenated standard ACSF (2.4 mM $CaCl_2$, 3 mM KCl, 129 mM NaCl, 20 mM $NaHCO_3$, 1.3 mM $MgSO_4$, 1.2 mM KH_2PO_4, and 10 mM glucose) at a rate of 2.5–3 mL/min at 32 ℃ that was maintained using an in-line solution heater (TC-344B, Warner Instruments). The pH of all ACSFs was set to 7.3–7.4, and the osmolarity was adjusted to 300–305 mOsm kg^{-1}. During slice preparation and electrophysiology recording, all solutions were continuously bubbled with 95% O_2/5% CO_2.

Whole-cell patch-clamp recordings were performed on visualized PO and VP neurons using a ×40 water-immersion lens (BX51WI, Olympus) and an infrared-sensitive charge-coupled device (CCD) camera. Patch pipettes (3–5 MΩ) were pulled from borosilicate glass capillaries (VitalSense Scientific Instruments Co., Ltd) using a four-stage horizontal micropipette puller (P1000, Sutter Instruments). Glass pipettes filled with intracellular solution containing 10 mM HEPES, 5 mM KCl, 130 mM K-gluconate, 0.6 mM EGTA, 2 mM $MgCl_2$, 2 mM Mg-ATP, and 0.3 mM Na-GTP (osmolarity: 285–290 mOsm/kg, pH: 7.2) were used for voltage-clamp recording. Signals were amplified with a Multiclamp 700B amplifier, low-pass filtered at 2.8 kHz, digitized at 10 kHz, and recorded in a computer for offline analysis using Clampfit 10.7 software (Molecular Devices). For recording light-evoked postsynaptic currents, blue light was delivered through an optical fiber (diameter of 200 μm, Inper) that was positioned 0.2 mm above the surface of the target areas. The membrane potentials were held at −70 mV for recording the excitatory postsynaptic currents and at 0 mV for recording inhibitory postsynaptic currents, and these recordings were immediately terminated once the series resistance changed more than 10%. To eliminate the polysynaptic components, tetrodotoxin (TTX; 1 μM, Dalian Refine Biochemical Items Co., Ltd.) and 4-aminopyridine (4-AP; 2 mM, Sigma)

were added to the standard ACSF to block sodium channels and augment light-induced postsynaptic currents, respectively.

von Frey and Hargreaves tests

In brief, the mice were habituated in a testing room for at least 3 days prior to testing to minimize stress. The mice were placed individually in transparent plastic chambers that were positioned on a wire mesh grid for 30 min each day. The mechanical withdrawal threshold was determined using a series of calibrated von Frey filaments. During measurement, these von Frey filaments were perpendicularly applied to the plantar surface of the hind paw or fore paw with sufficient force to bend the filaments. The minimal force filament that induced the mice to present a brisk paw withdrawal, flinching, or licking was taken as the mechanical response threshold. If there was no positive pain response, a filament with a greater force was applied, and the measurement was repeated five times to obtain an average threshold.

The thermal nociceptive threshold was assessed using the Hargreaves test. After habituation, radiant laser heat (IITC, CA, USA) was delivered to the paw, and the latency of paw withdrawal was measured. The basal paw withdrawal latency was adjusted to 9–12 s and the thermal laser stimulation on the paw lasted for only 20 s to avoid potential tissue damage. During optogenetic experiments, nociceptive thresholds were tested for about 1 min following light delivery.

Intrathecal naloxone injection

The isoflurane-anesthetized mice were held firmly from the pelvic girdle. A 27-gauge injection needle attached to a 25 μL Hamilton microliter syringe was punctured into the intervertebral space between L5 and L6 lumbar vertebrae until a tail flick was observed. Next, 10 μL of naloxone (Sigma, 0.2 mg/kg in ACSF) or vehicle (ACSF) was administered intrathecally at a rate of 5 μL/ min 30 min before von Frey and Hargreaves tests. The needle was kept in place for at least 1 min to prevent the fluid withdrawal. After drug delivery, the mice were rapidly transferred to a wire mesh grid for habitation.

Open field test

To determine the effect of white noise on anxiety-like behavior, the mice were individually placed in one corner of an open field apparatus (50 cm × 50 cm × 30 cm) and were allowed to freely explore the apparatus for 5 min immediately after noise exposure, and the movement trajectories were recorded by a video camera. The square area at the center of the apparatus (25 cm × 25 cm) was defined as the center zone, and the time spent in this central area was offline

analyzed using EthoVision XT software. The apparatus was cleaned using 75% ethanol after each testing to remove odor cues.

Light-dark box test

The light-dark boxes consisted of a light chamber and a dark one of equal size (20 cm × 15 cm × 30 cm). The two chambers were separated by a wall with an open gate (5 cm × 5 cm) to allow the mice to freely explore the two chambers. To test the effect of white noise on anxiety-like behavior, the mice were individually placed in the light chamber and allowed to freely explore the apparatus for 15 min immediately following noise exposure. The travel trajectories were video-recorded and offline analyzed using EthoVision XT software. The time spent in each chamber was calculated.

Elevated plus maze test

The apparatus, which consisted of a central platform (6× 6 cm) and two open arms (30× 6 cm) orthogonal to two closed arms (30× 6× 20 cm), was placed 100 cm above the floor. Each mouse was placed on the central platform toward a closed arm and allowed to explore the maze for 5 min. The movement trajectory of mice was video-recorded using a camera from above. The time spent in the open arms and the number of entries into the open arms were analyzed offline using EthoVision XT software (Noldus).

Real-time place avoidance and conditioned place preference tests

The light-dark boxes were also used to evaluate aversion scores caused by subthreshold stimuli. In brief, an apparatus without a bottom floor was placed on a wire mesh grid. The mice were placed in the light chamber and allowed to freely explore the apparatus for 15 min (Pre). Then, subthreshold von Frey stimuli were applied to the intact hindpaw once the mice entered the light chamber, and they were applied to the CFA-treated paw once the mice entered the dark chamber for 15 min (During). The stimulus was applied once every 2 s. To test whether white noise exposure had an effect on subthreshold stimulation induced aversion, the mice were allowed to first explore the apparatus for 15 min with subthreshold von Frey stimuli application. Then, sound was delivered for 10 min, and the mice were allowed to explore the apparatus without any other stimuli. In the During section, white noise was constantly delivered with 0.04 g von Frey stimuli applied for 15 min. The avoidance ratio was calculated by dividing the time spent in the During period by that in the Pre period.

An apparatus consisting of two chambers (40 × 20 cm) connected by a ‘neck’ structure was used to examine the sound delivery and optogenetic manipulation-induced preference. Mice were firstly allowed to explore the apparatus for 15 min without any stimulation. The time spent in each chamber on the first day was calculated and the chamber

with the lesser spending time was selected as the stimulation side. On the following consecutive 3 days, mice were allowed to freely explore the apparatus for 20 min daily, and sound or light was only delivered when the mice entered the stimulation side and continued until the mice remained in the stimulation-paired compartment. On the day 5, a 15-min preference test was performed by allowing mice to freely explore the apparatus without any stimulation. Mice movements were video-recorded and the time spent in the dark chamber was analyzed offline using EthoVision XT software. The preference ratio was calculated as the time in the stimulation-paired side on the 5th day to that on the 1st day.

Serum corticosterone measurement

Fifteen min following sound treatment, mice were anesthetized for blood harvesting from the orbital sinus. The blood samples were allowed to clot before centrifugation at 3000×g for 20 min at 4 ℃. Supernatants were collected and stored −20 °C assays. Serum corticosterone level was measured using a correlate-enzyme immunoassay kit (CSB-E07969m, CUSABIO, Wuhan, China) following manufacturer's instructions. Briefly, the microtiter plate provided in the kit was pre-coated with goat anti-rabbit antibody. Standards or serum samples were added to the appropriate microtiter plate wells with an antibody specific for corticosterone and horseradish peroxidase conjugated corticosterone. Then, the substrate was added to react with the bound corticosterone-peroxidase conjugate. After incubation for 15 min, the reaction was read at 450 nm.

Immunohistochemistry and imaging

First, the mice were deeply anesthetized using pentobarbital (20 mg/kg, i.p.) and transcardially perfused with 0.9% saline, followed by 4% paraformaldehyde in phosphate buffer (0.1 M). After perfusion, the brain was carefully removed and post-fixed in 4% PFA at 4 ℃ for at least 24 h. Following cryoprotection in a 30% (w/v) sucrose solution, coronal sections (40 μm) were prepared using a cryostat (Leica CM1860, Germany), and the slices were stored in a cryoprotectant solution containing 30% glycerol (v/v), 20% ethylene glycol (v/v), and PBS at −20°C for future staining or imaging. For immunohistochemistry, these slices were first incubated in 0.3% (v/v) Triton X-100 for 30 min, followed by blocking of non-specific reactions with 10% donkey serum for 1 h at room temperature. Then, these slices were incubated with appropriate primary antibodies diluted in blocking solution (0.3% Triton X-100, 10% donkey serum in PBS) at 4 ℃ for 24 h. The primary antibodies included: anti-glutamate (1:500, rabbit, Sigma, G6642) and anti-GABA (1:500, rabbit, Sigma, A2052). After washing with PBS (3 × 5 min), these slices were incubated with the corresponding fluorophore-conjugated secondary antibodies (1:500, Invitrogen) for 2 h at room temperature. Finally, these slices were incubated with 4,6-diamidino-2-phenylindole (DAPI; 1:2,000, Sigma) for 5 min and then washed

with PBS three times and mounted for imaging. The fluorescence signals were imaged using either a Zeiss LSM880 or an Olympus FV1200S microscope. The fluorescent intensity of presynaptic terminals originating from ACx^{Glu} neurons was quantified using ImageJ software (NIH). Each brain section was converted to an 8-bit image and the brain regions of interest were encompassed by manually drawing a selection outline according to the brain atlas. Then, the fluorescence density was computed by blindly counting the sum of the gray values of all pixels in the selection and dividing by the number of pixels. The axon density in each brain structure was normalized to the average fluorescence density in the VP from ACx^{Glu} neurons.

Statistical analysis

The data obtained from the mice with missed injections or optical fiber placement were excluded from further analysis by experimenters who were blinded to the experimental conditions. Major experiments were successfully repeated in the lab for at least two times. Data describe biological replicates. The Shapiro-Wilk test was used to check the normality of data. Nonparametric Mann-Whitney U test or Wilcoxon matched-paired signed rank test was performed if data were not normally distributed. A paired or unpaired two-tailed Student's *t*-test was conducted for the statistical comparisons of data between two groups. One- or two-way analysis of variance (ANOVA) was conducted for statistical evaluation of data among more than two groups. Geisser–Greenhouse correction was applied to the data to ensure equal variability of difference in ANOVA, which was followed by Bonferroni post-hoc test for multiple comparisons between groups. The sample sizes in our study were not predetermined by any statistical methods but were similar to previous publications. All data in this study are presented as the mean ± s.e.m. The significance levels are indicated as $*P < 0.05$, $**P < 0.01$, and $***P < 0.001$. GraphPad Prism 8 (Graph Pad Software, Inc.) was used for statistical analyses and graphing.

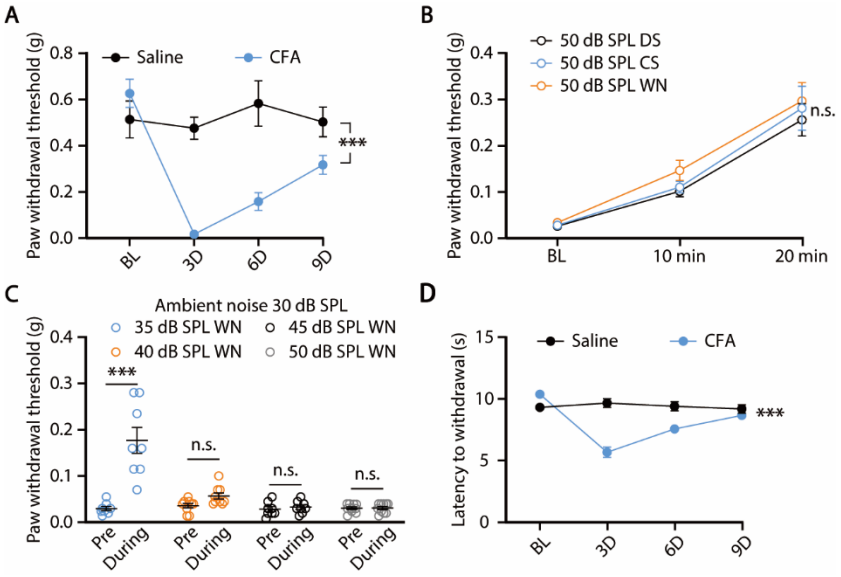
A
Paw withdrawal threshold (g)
Saline
CFA
***
BL
3D
6D
9D
B
Paw withdrawal threshold (g)
50 dB SPL DS
50 dB SPL CS
50 dB SPL WN
n.s.
BL
10 min
20 min
C
Ambient noise 30 dB SPL
35 dB SPL WN
40 dB SPL WN
45 dB SPL WN
50 dB SPL WN
Paw withdrawal threshold (g)
***
n.s.
n.s.
n.s.
Pre
During
D
Latency to withdrawal (s)
Saline
CFA
***
BL
3D
6D
9D

Fig. S1. Low-intensity sound relative to ambient noise increases mechanical nociceptive threshold in CFA mice.

(**A**) The mechanical nociceptive threshold of mice treated with saline or CFA based on the von Frey test (n = 10 mice; Saline, n = 9 mice; $F_{3,51} = 9.696$, $P < 0.0001$). (**B**) The mechanical nociceptive threshold of CFA mice exposed to 50 dB SPL consonant sound (CS), dissonant sound (DS), and white noise (WN) (CS, n = 10 mice; DS, n = 10 mice; WN, n = 9 mice; $F_{4,52} = 0.2424$, $P = 0.9129$). (**C**) The mechanical nociceptive threshold of CFA mice exposed to white noise at different intensities in an environment with ambient noise at 30 dB SPL (35 dB SPL, n = 8 mice; 40 dB SPL, n = 9 mice; 45 dB SPL, n = 8 mice; 50 dB SPL, n = 8 mice; $F_{3,31} = 21.50$, $P < 0.0001$). (**D**) The thermal nociceptive threshold of mice treated with saline or CFA in the Hargreaves test (n = 10 mice each group; $F_{3,54} = 33.78$, $P < 0.0001$). The data are expressed as the mean ± s.e.m. $^{**}P < 0.01$; $^{***}P < 0.001$. n.s., not significant. Details of the statistical analyses are presented in table S2.

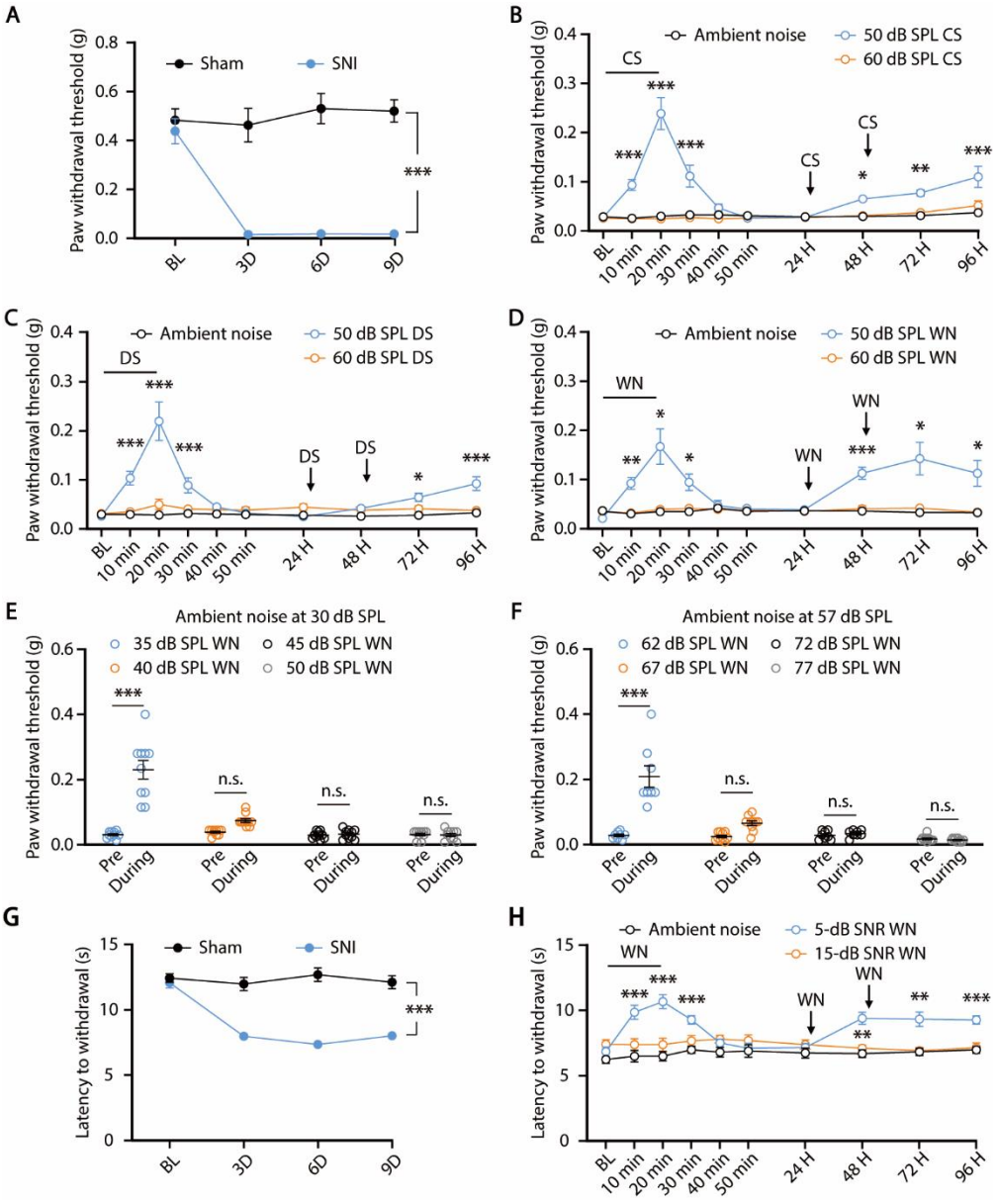
A
Paw withdrawal threshold (g)
Sham
SNI
***
BL
3D
6D
9D
B
Ambient noise
50 dB SPL CS
60 dB SPL CS
CS
Paw withdrawal threshold (g)
BL
10 min
20 min
30 min
40 min
50 min
24 H
48 H
72 H
96 H
C
Ambient noise
50 dB SPL DS
60 dB SPL DS
DS
Paw withdrawal threshold (g)
D
Ambient noise
50 dB SPL WN
60 dB SPL WN
WN
Paw withdrawal threshold (g)
E
Ambient noise at 30 dB SPL
35 dB SPL WN
40 dB SPL WN
45 dB SPL WN
50 dB SPL WN
Paw withdrawal threshold (g)
n.s.
Pre
During
F
Ambient noise at 57 dB SPL
62 dB SPL WN
67 dB SPL WN
72 dB SPL WN
77 dB SPL WN
Paw withdrawal threshold (g)
G
Sham
SNI
Latency to withdrawal (s)
H
Ambient noise
5-dB SNR WN
15-dB SNR WN
WN
Latency to withdrawal (s)

Fig. S2. The effects of different sound on nociceptive thresholds in SNI mice.

(**A**) The mechanical nociceptive threshold of mice treated with sham or SNI (sham, n = 8 mice; SNI, n = 9 mice; $F_{3,45} = 12.25$, $P < 0.0001$). (**B** to **D**) The mechanical nociceptive threshold of SNI mice treated with or without CS (B, ambient noise, n = 10 mice; 50 dB SPL, n = 10 mice; 60 dB SPL, n = 8 mice; $F_{18,250} = 14.72$, $P < 0.0001$), DS (C, ambient noise, n = 10 mice; 50 dB SPL, n = 8 mice; 60 dB SPL, n = 8 mice; $F_{18,230} = 12.6$, $P < 0.0001$), and white noise (D, ambient noise, n = 10 mice; 50 dB SPL, n = 8 mice; 60 dB SPL, n = 7 mice; $F_{18,198} = 7.238$, $P < 0.0001$) in an environment with ambient noise at 45 dB SPL. (**E** and **F**) The mechanical nociceptive threshold of SNI mice exposed to white noise at different intensities in an environment with ambient noise at 30 dB SPL (E, 35 dB SPL, n = 10 mice; 40 dB SPL, n = 10 mice; 45 dB SPL, n = 10 mice; 50 dB SPL, n = 10 mice; $F_{3,36} = 39.96$, $P < 0.0001$) or 57 dB SPL (F, 62 dB SPL, n = 8 mice; 67 dB SPL, n = 10 mice; 72 dB SPL, n = 8 mice; 77 dB SPL, n = 10 mice; $F_{3,32} = 27.10$, $P < 0.0001$). (**G**) The thermal nociceptive threshold of mice treated with sham or SNI (n = 10 mice each group; $F_{3,54} = 16.44$, $P < 0.0001$). (**H**) The thermal nociceptive threshold of SNI mice treated with different SNR white noise (n = 10 mice each group; $F_{18,243} = 5.043$, $P < 0.0001$). The data are expressed as the mean ± s.e.m. *$P < 0.05$; **$P < 0.01$; ***$P < 0.001$. n.s., not significant. Details of the statistical analyses are presented in table S2.

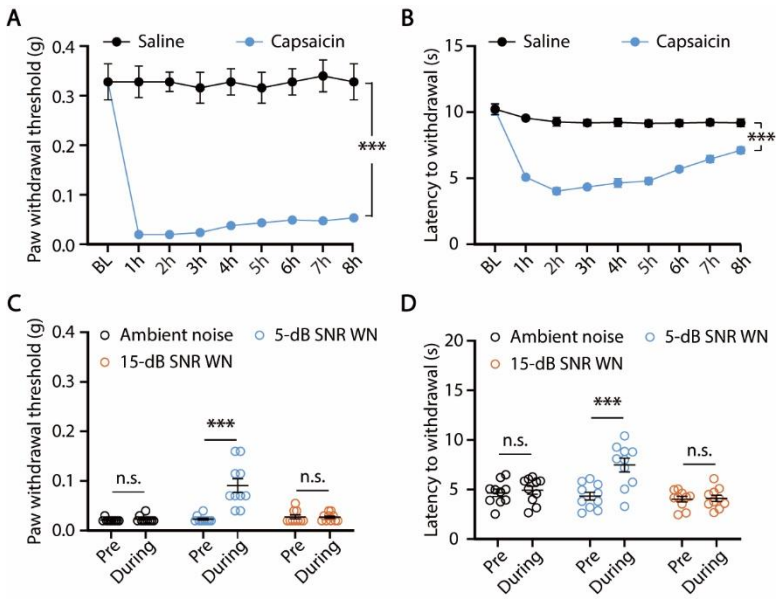
A
Saline
Capsaicin
Paw withdrawal threshold (g)
0.4
0.3
0.2
0.1
0.0
***
BL
1h
2h
3h
4h
5h
6h
7h
8h
B
Saline
Capsaicin
Latency to withdrawal (s)
15
10
5
0
***
BL
1h
2h
3h
4h
5h
6h
7h
8h
C
Ambient noise
5-dB SNR WN
15-dB SNR WN
Paw withdrawal threshold (g)
0.4
0.3
0.2
0.1
0.0
n.s.
***
n.s.
Pre
During
Pre
During
Pre
During
D
Ambient noise
5-dB SNR WN
15-dB SNR WN
Latency to withdrawal (s)
20
15
10
5
0
n.s.
***
n.s.
Pre
During
Pre
During
Pre
During

Fig. S3. Low SNR sound increases nociceptive thresholds in mice treated with capsaicin.

(**A** and **B**) The mechanical (A, n = 10 mice each group; $F_{8,144} = 21.90$, $P < 0.0001$) and thermal (B, n = 10 mice each group; $F_{8,144} = 18.94$, $P < 0.0001$) nociceptive thresholds in mice treated with saline or capsaicin. (**C** and **D**) The mechanical (C, n = 10 mice each group; ambient noise, Pre vs. During, $W = 3$, $P = 0.5$; 5-dB SNR, Pre vs. During, $W = 55$, $P = 0.002$; 15-dB SNR, Pre vs. During, $W = -2$, $P > 0.9999$) and thermal (D, n = 10 mice each group; $F_{2,27} = 10.21$, $P = 0.0005$) nociceptive thresholds of capsaicin-treated mice exposed to different SNR white noise. The data are expressed as the mean ± s.e.m. ***$P < 0.001$. n.s., not significant. All statistical measure details are presented in table S2.

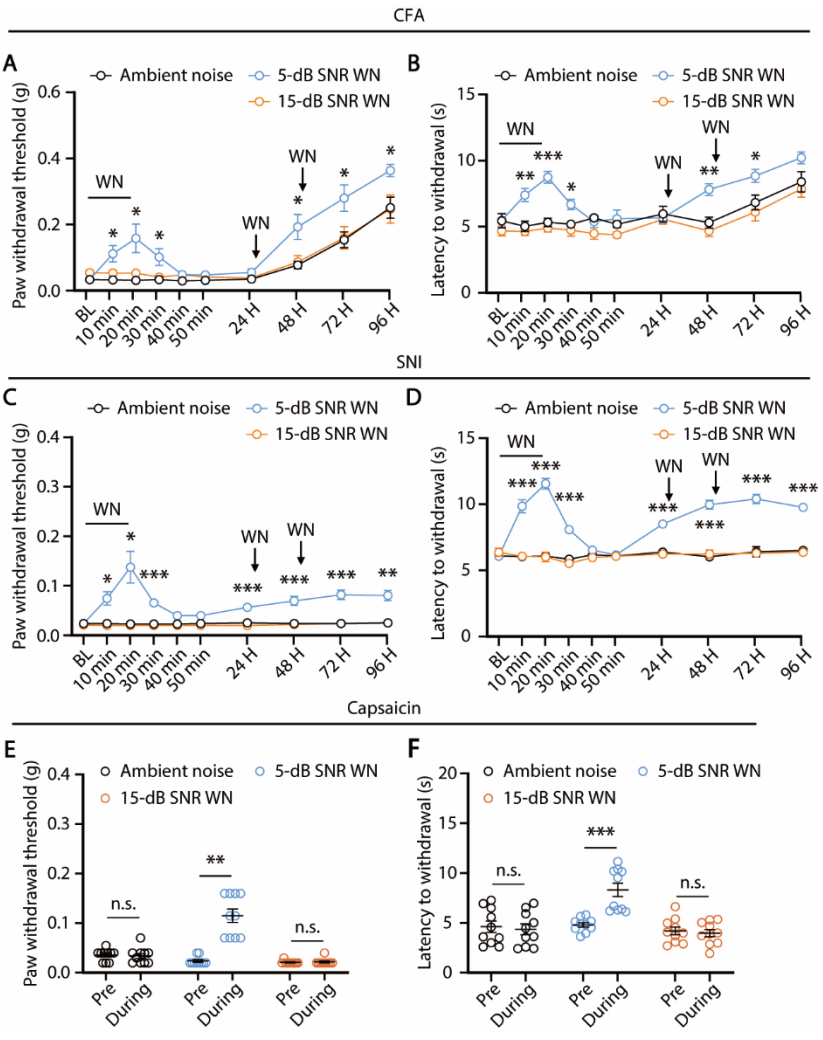
CFA
A
Ambient noise
5-dB SNR WN
15-dB SNR WN
Paw withdrawal threshold (g)
WN
BL
10 min
20 min
30 min
40 min
50 min
24 H
48 H
72 H
96 H
B
Latency to withdrawal (s)
SNI
C
D
Capsaicin
E
F
n.s.
Pre
During

Fig. S4. Low SNR sound increases nociceptive thresholds in female mice with different types of pain.

(**A** and **B**) The mechanical (A, n = 10 mice each group; $F_{18,243} = 2.553$, $P = 0.0007$) and thermal (B, n = 10 mice each group; $F_{18,243} = 2.639$, $P = 0.0004$) nociceptive thresholds in female CFA mice exposed to different SNR white noise. (**C** and **D**) The mechanical (C, n = 10 mice each group; $F_{18,243} = 6.572$, $P < 0.0001$) and thermal (D, ambient noise, n = 10 mice; 5-dB SNR, n = 9 mice; 15-dB SNR, n = 10 mice; $F_{18,225} = 17.99$, $P < 0.0001$) nociceptive thresholds in female SNI mice exposed to different SNR white noise. (**E** and **F**) The mechanical (E, n = 10 mice each group; ambient noise, Pre vs. During, W = -2, P = 0.75; 5-dB SNR, Pre vs. During, W = 55, P = 0.002; 15-dB SNR, Pre vs. During, W = 1, P >0.9999) and thermal (F, n = 10 mice each group; $F_{2,27} = 16.97$, $P < 0.0001$) nociceptive thresholds in capsaicin female mice exposed to different SNR white noise. The data are expressed as the mean ± s.e.m. *$P < 0.05$; **$P < 0.01$; ***$P < 0.001$. n.s., not significant. Details of the statistical analyses are presented in table S2.

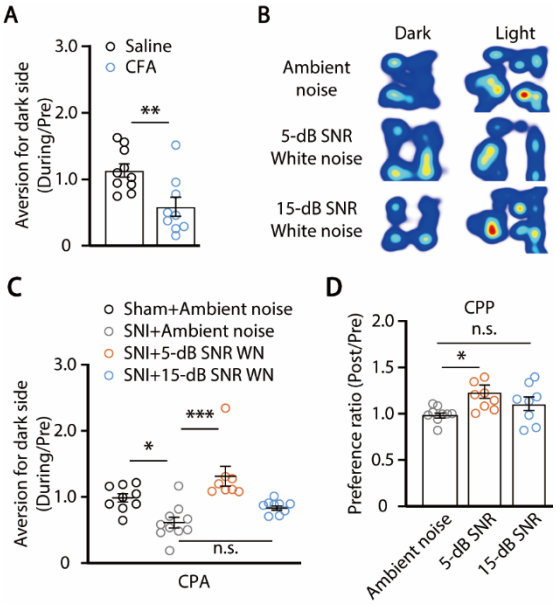
A
Saline
CFA
Aversion for dark side (During/Pre)
3.0
2.0
1.0
0
**
B
Dark
Light
Ambient noise
5-dB SNR White noise
15-dB SNR White noise
C
Sham+Ambient noise
SNI+Ambient noise
SNI+5-dB SNR WN
SNI+15-dB SNR WN
Aversion for dark side (During/Pre)
*
***
n.s.
CPA
D
CPP
n.s.
*
Preference ratio (Post/Pre)
2.0
1.5
1.0
0.5
0
Ambient noise
5-dB SNR
15-dB SNR

Fig. S5. Low SNR sound reduces the place aversion in SNI mice.

(**A**) Summarized data for place aversion in the CPA test from the indicated group (Saline, n = 10 mice; CFA, n = 9 mice; $t_{17} = 3.22$, $P = 0.005$). (**B**) Representative heatmaps of travel trajectory of CFA mice treated with ambient noise, 5-dB or 15-dB SNR white noise in the CPA test. (**C**) Summarized data for place aversion of SNI mice from the indicated group (ambient noise, n = 11 mice; 5-dB SNR, n = 10 mice; 15-db SNR, n = 8 mice; $F_{3,32} = 10.92$, $P < 0.0001$). (D) Summarized data of the preference for sound-delivery side from SNI mice treated with different SNR white noise (Sham + ambient noise, n = 9 mice; SNI + ambient noise, n = 10 mice; SNI + 5-dB SNR WN, n = 8 mice; SNI + 15-dB SNR WN, n = 9 mice; $F_{2,23} = 4.732$, $P = 0.019$). The data are expressed as the mean ± s.e.m. *$P < 0.05$; **$P < 0.01$; ***$P < 0.001$. n.s., not significant. Details of the statistical analyses are presented in table S2.

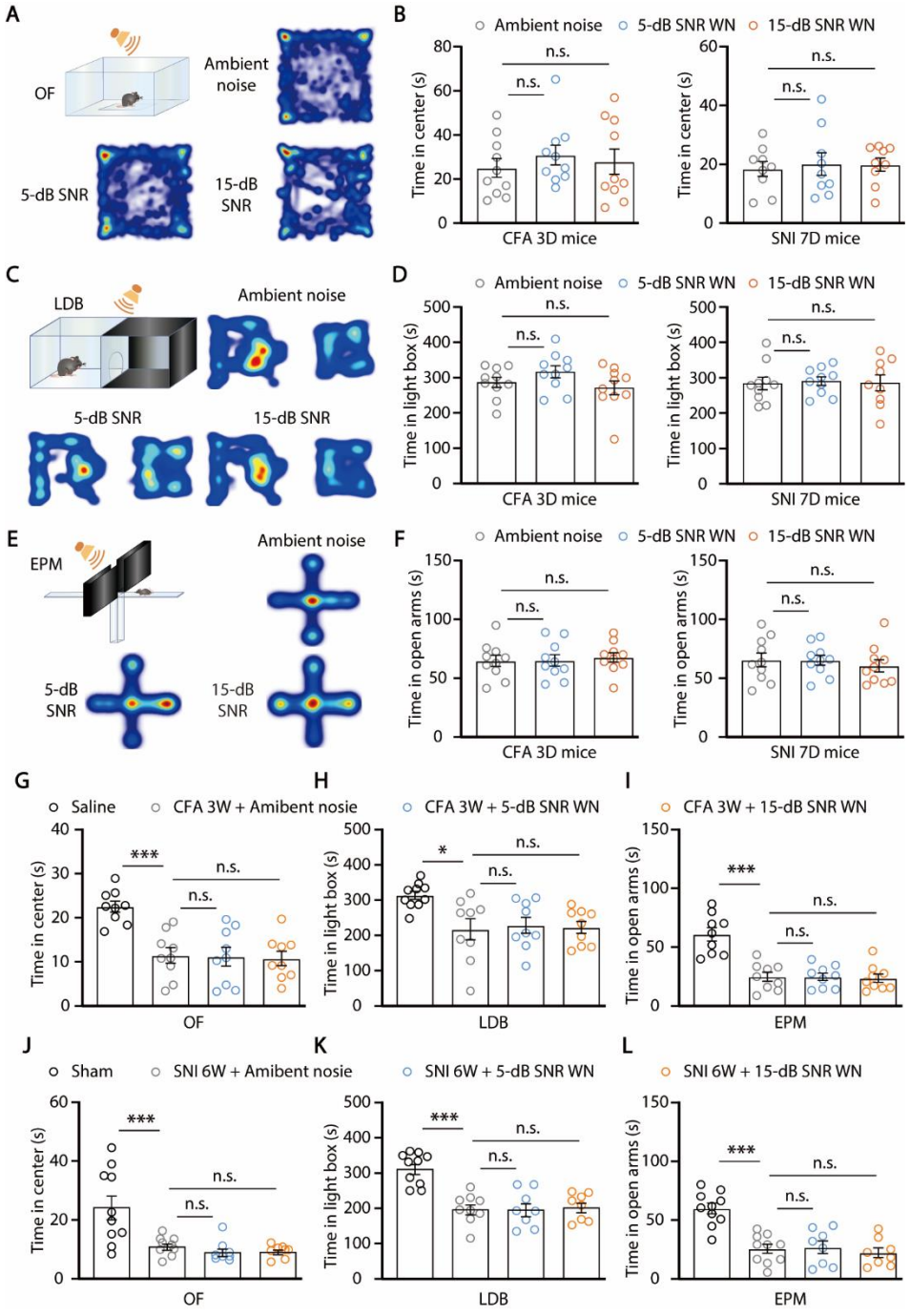
A
OF
Ambient noise
5-dB SNR
15-dB SNR
B
Ambient noise
5-dB SNR WN
15-dB SNR WN
Time in center (s)
n.s.
CFA 3D mice
SNI 7D mice
C
LDB
Ambient noise
5-dB SNR
15-dB SNR
D
Time in light box (s)
E
EPM
F
Time in open arms (s)
G
Saline
CFA 3W + Amibent nosie
***
*
H
CFA 3W + 5-dB SNR WN
I
CFA 3W + 15-dB SNR WN
OF
LDB
EPM
J
Sham
SNI 6W + Amibent nosie
K
SNI 6W + 5-dB SNR WN
L
SNI 6W + 15-dB SNR WN

Fig. S6. Neither 5-dB nor 15-dB SNR white noise affects anxiety-like behaviors in CFA and SNI mice.

(**A** and **B**) Schematic for open field (OF) test and heatmaps of the travel trajectory from the indicated group (A), and summarized data for time spent in center from CFA 3d mice (B, left, n = 10 mice each group; $F_{2,27} = 0.3616$, $P = 0.6999$) and SNI 7de mice (B, right, n = 9 mice each group; $F_{2,24} = 0.0978$, $P = 0.9072$). (**C** and **D**) Schematic for light-dark box (LDB) test and heatmaps of the travel trajectory from the indicated group (C), and summarized data for time spent in light box from CFA 3d mice (D, left, n = 10 mice each group; $F_{2,27} = 1.856$, $P = 0.1757$) and SNI 7d mice (D, right, ambient noise, n = 10 mice; 5-dB SNR, n = 10 mice; 15-dB SNR, n = 9 mice; $F_{2,26} = 0.040$, $P = 0.961$). (**E** and **F**) Schematic for elevated plus maze (EPM) test and heatmaps of the travel trajectory from the indicated group (E), and summarized data for time spent in open arms from CFA 3d mice (F, left, n = 10 mice each group; $F_{2,27} = 0.1227$, $P = 0.885$) and SNI 7d mice (F, right, n = 10 mice each group; $F_{2,27} = 0.3026$, $P = 0.7413$). (**G** to **I**) Summarized data for CFA 3W mice exposed to different white noise in OF (G, n = 9 mice each group; $F_{3,32} = 11.12$, $P < 0.0001$), LDB (H, Saline, n = 9 mice; ambient noise, n = 10 mice; 5-dB SNR, n = 9 mice; 15-dB SNR, n = 9 mice; $F_{3,33} = 5.026$, $P = 0.0056$), and EPM tests (I, n = 9 mice each group; $F_{3,32} = 19.07$, $P < 0.0001$). (**J** to **L**) Summarized data for SNI 6W mice exposed to different white noise in OF (J, Sham, n = 10 mice; ambient noise, n = 9 mice; 5-dB SNR, n = 8 mice; 15-dB SNR, n = 8 mice; $F_{3,31} = 9.507$, $P = 0.0001$), LDB (K, Sham, n = 10 mice; ambient noise, n = 9 mice; 5-dB SNR, n = 8 mice; 15-dB SNR, n = 8 mice; $F_{3,31} = 15.47$, $P < 0.0001$), and EPM tests (L, Sham, n = 10 mice; ambient noise, n = 10 mice; 5-dB SNR, n = 8 mice; 15-dB SNR, n = 8 mice; $F_{3,32} = 16.64$, $P < 0.0001$). The data are expressed as the mean ± s.e.m. n.s., not significant. Details of the statistical analyses are presented in table S2.

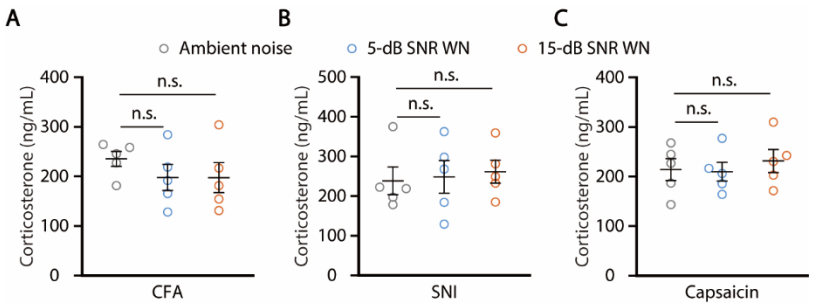
A
B
C
Ambient noise
5-dB SNR WN
15-dB SNR WN
Corticosterone (ng/mL)
400
300
200
100
0
n.s.
n.s.
CFA
500
SNI
Capsaicin

Fig. S7. Neither 5-dB nor 15-dB SNR white noise affects the serum corticosterone level in mice with different types of pain.

(**A** to **C**) Summarized data for serum corticosterone levels in CFA- (A, n = 5 mice each group; $F_{2,12} = 0.7843$, $P = 0.4785$), SNI- (B, n = 5 mice each group; $F_{2,12} = 0.1050$, $P = 0.9012$), or capsaicin-treated (C, n = 5 mice each group; $F_{2,12} = 0.2805$, $P = 0.7602$) mice after exposure to different SNR white noise. The data are expressed as the mean ± s.e.m. n.s., not significant. Details of the statistical analyses are presented in table S2.

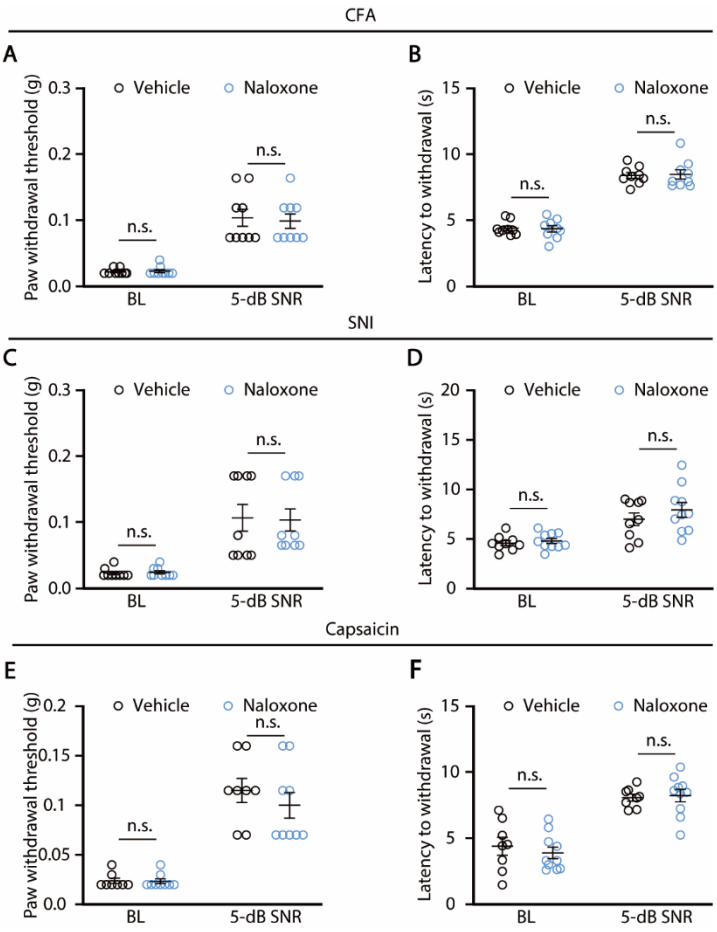
CFA
A
B
Vehicle
Naloxone
Paw withdrawal threshold (g)
Latency to withdrawal (s)
n.s.
BL
5-dB SNR
SNI
C
D
Capsaicin
E
F

Fig. S8. Effects of naloxone on low SNR sound-induced increase in nociceptive thresholds.

(**A** and **B**) Summarized data for mechanical (A, n = 9 mice each group; BL, vehicle vs. naloxone, U = 39.5, P >0.9999; 5-dB SNR, vehicle vs. naloxone, U = 38.5, P = 0.9914) and thermal (B, vehicle, n = 10 mice; naloxone, n = 9 mice; $F_{1,16}$ = 0.04835, P = 0.8287) nociceptive thresholds in CFA mice with intrathecal injection of naloxone or vehicle before and after 5-dB SNR white noise exposure. (**C** and **D**) Summarized data for mechanical (C, n = 10 mice each group; BL, vehicle vs. naloxone, U = 36.5, P = 0.9294; 5-dB SNR, vehicle vs. naloxone, U = 35, P = 0.6686) and thermal (D, vehicle, n = 9 mice; naloxone, n = 10 mice; $F_{1,16}$ = 0.5337, P = 0.475) nociceptive thresholds in naloxone-treated SNI mice exposed to 5-dB SNR white noise. (**E** and **F**) Summarized data for mechanical (E, vehicle, n = 8 mice; naloxone, n = 9 mice; BL, vehicle vs. naloxone, U = 35, P >0.9999; 5-dB SNR, vehicle vs. naloxone, U = 27, P = 0.4552) and thermal (F, n = 10 mice each group; $F_{1,16}$ = 0.698, P = 0.4158) nociceptive thresholds in naloxone-treated capsaicin SNI mice exposed to 5-dB SNR white noise. The data are expressed as the mean ± s.e.m. n.s., not significant. Details of the statistical analyses are presented in table S2.

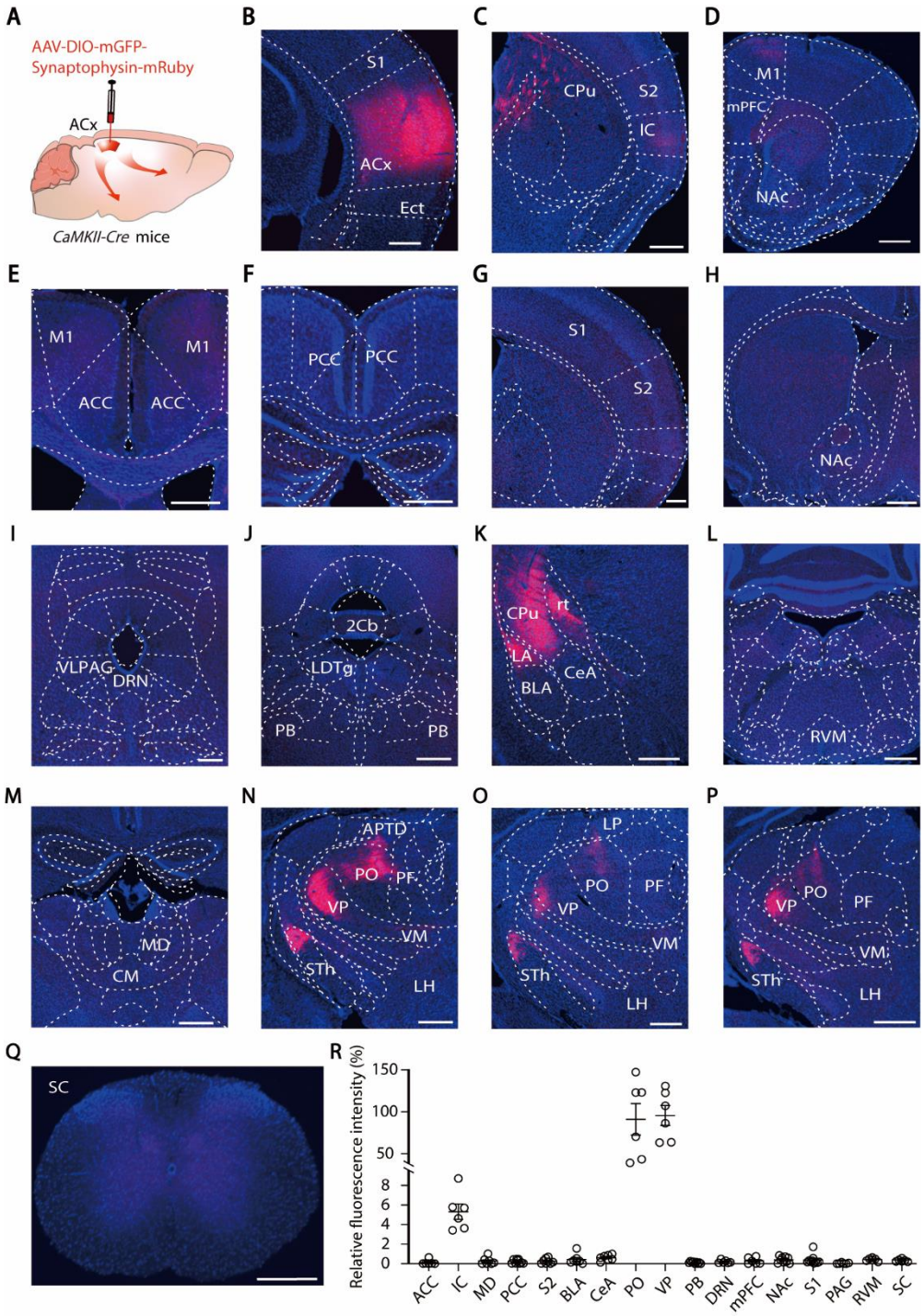
A
AAV-DIO-mGFP-
Synaptophysin-mRuby
ACx
CaMKII-Cre mice
B
S1
ACx
Ect
C
CPu
S2
IC
D
M1
mPFC
NAc
E
M1
M1
ACC
ACC
F
PCC
PCC
G
S1
S2
H
NAc
I
VLPAG
DRN
J
2Cb
LDTg
PB
PB
K
CPu
rt
LA
BLA
CeA
L
RVM
M
MD
CM
N
APTD
PO
PF
VP
VM
STh
LH
O
LP
PO
PF
VP
VM
STh
LH
P
VP
PO
PF
VM
STh
LH
Q
SC
R
Relative fluorescence intensity (%)
150
100
50
8
6
4
2
0
ACC
IC
MD
PCC
S2
BLA
CeA
PO
VP
PB
DRN
mPFC
NAc
S1
PAG
RVM
SC

Fig. S9. Outputs of ACx^{Glu} neurons.

(**A**) Schematic of viral injection in the ACx of *CaMKII-Cre* mice. (**B**) A representative image of viral expression in the ACx of *CaMKII-Cre* mice. Scale bar, 500 μm. (**C** to **Q**) Representative images of mRuby signals and summarized data for their relative fluorescence intensities in the indicated regions. CPu, caudate putamen; ICx, insular cortex; M1, primary motor cortex; STh, subthalamic nucleus; LA, lateral amygdala; ACC, anterior cingulate cortex; PCC, posterior cingulate cortex; mPFC, medial prefrontal cortex; S1, primary somatosensory cortex; S2, secondary somatosensory cortex; MD, mediodorsal thalamic nucleus; CM, central medial thalamic nucleus; BLA, basolateral amygdala; CeA, central amygdala; VLPAG, ventrolateral periaqueductal gray; NAc, nucleus accumbens; DRN, dorsal raphe nucleus; PB, parabrachial nucleus; RVM, rostral ventromedial medulla; SC, spinal cord; PF, parafascicular thalamic nucleus; VM, ventromedial thalamic nucleus; STh, subthalamic nucleus; ECt, ectorhinal cortex; LDTg, laterodorsal tegmental nucleus; rt, reticular thalamic nucleus; LH, lateral hypothalamic area; LP, lateral posterior thalamic nucleus. Scale bars, 500 μm.

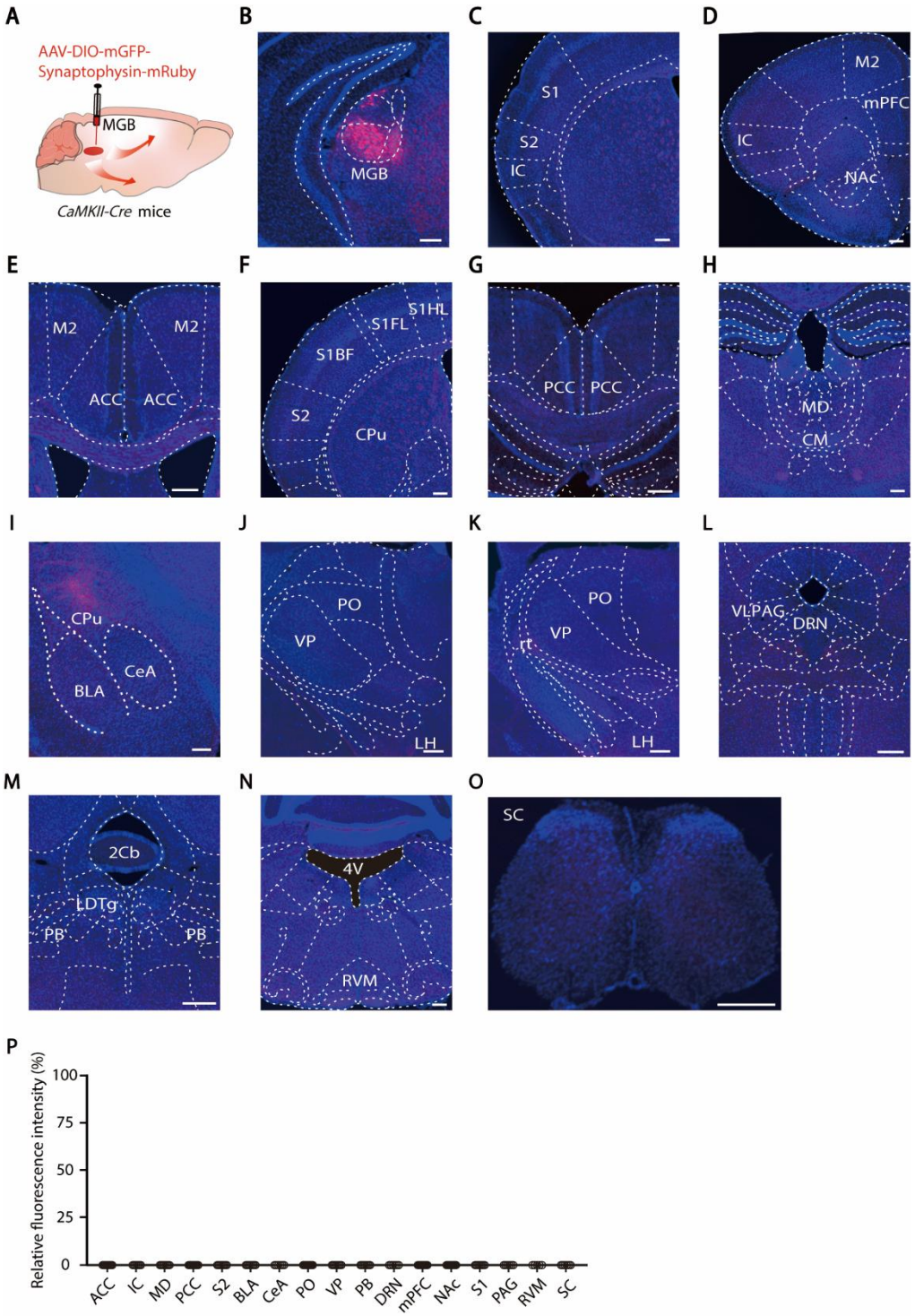
A
AAV-DIO-mGFP-Synaptophysin-mRuby
MGB
CaMKII-Cre mice
B
MGB
C
S1
S2
IC
D
M2
mPFC
IC
NAc
E
M2
M2
ACC
ACC
F
S1HL
S1FL
S1BF
S2
CPu
G
PCC
PCC
H
MD
CM
I
CPu
CeA
BLA
J
PO
VP
LH
K
PO
VP
rt
LH
L
VLPAG
DRN
M
2Cb
LDTg
PB
PB
N
4V
RVM
O
SC
P
Relative fluorescence intensity (%)
100
75
50
25
0
ACC
IC
MD
PCC
S2
BLA
CeA
PO
VP
PB
DRN
mPFC
NAc
S1
PAG
RVM
SC

Fig. S10. Outputs of MGB^{Glu} neurons.

(**A**) Schematic of viral injection in the MGB of *CaMKII-Cre* mice. (**C** to **P**) Representative images of mRuby signals and summarized data for their relative fluorescence intensities in the indicated regions.

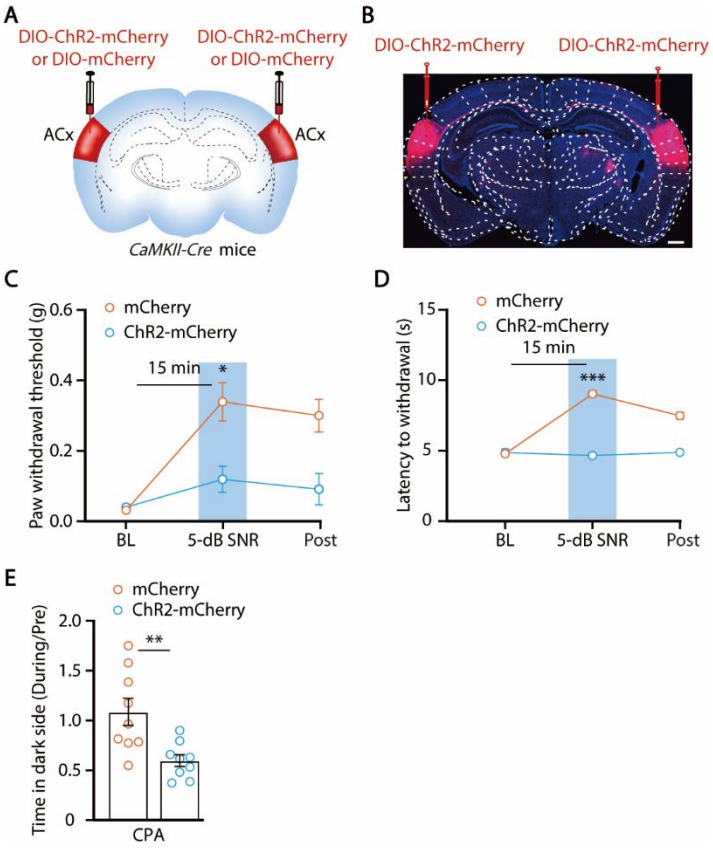
A
DIO-ChR2-mCherry or DIO-mCherry
DIO-ChR2-mCherry or DIO-mCherry
ACx
ACx
CaMKII-Cre mice
B
DIO-ChR2-mCherry
DIO-ChR2-mCherry
C
Paw withdrawal threshold (g)
0.6
0.4
0.2
0.0
mCherry
ChR2-mCherry
15 min
*
BL
5-dB SNR
Post
D
Latency to withdrawal (s)
15
10
5
0
mCherry
ChR2-mCherry
15 min
***
BL
5-dB SNR
Post
E
Time in dark side (During/Pre)
2.0
1.5
1.0
0.5
0
mCherry
ChR2-mCherry
**
CPA

Fig. S11. Activation of ACx^{Glu} neurons blocks 5-dB SNR-induced effects on nociceptive thresholds and place aversion.

(**A**) Schematic of viral injection for optogenetic manipulations. (**B**) A representative image of DIO-ChR2-mCherry expression in the ACx of *CaMKII-Cre* mice. Scale bar, 500 μm. (**C** to **E**) Summarized data for mechanical (C, $n = 8$ mice each group; $F_{2,28} = 8.849$, $P = 0.0011$), thermal nociceptive thresholds (D, $n = 10$ mice each group; $F_{2,36} = 102.2$, $P < 0.0001$) and place aversion (E, $n = 9$ mice each group; $t_{16} = 3.323$, $P = 0.0043$) in CFA mice exposed to 5-dB SNR white noise during optical activation of ACx^{Glu} neurons. The data are expressed as the mean ± s.e.m. *$P < 0.05$; **$P < 0.01$. n.s., not significant. Details of the statistical analyses are presented in table S2.

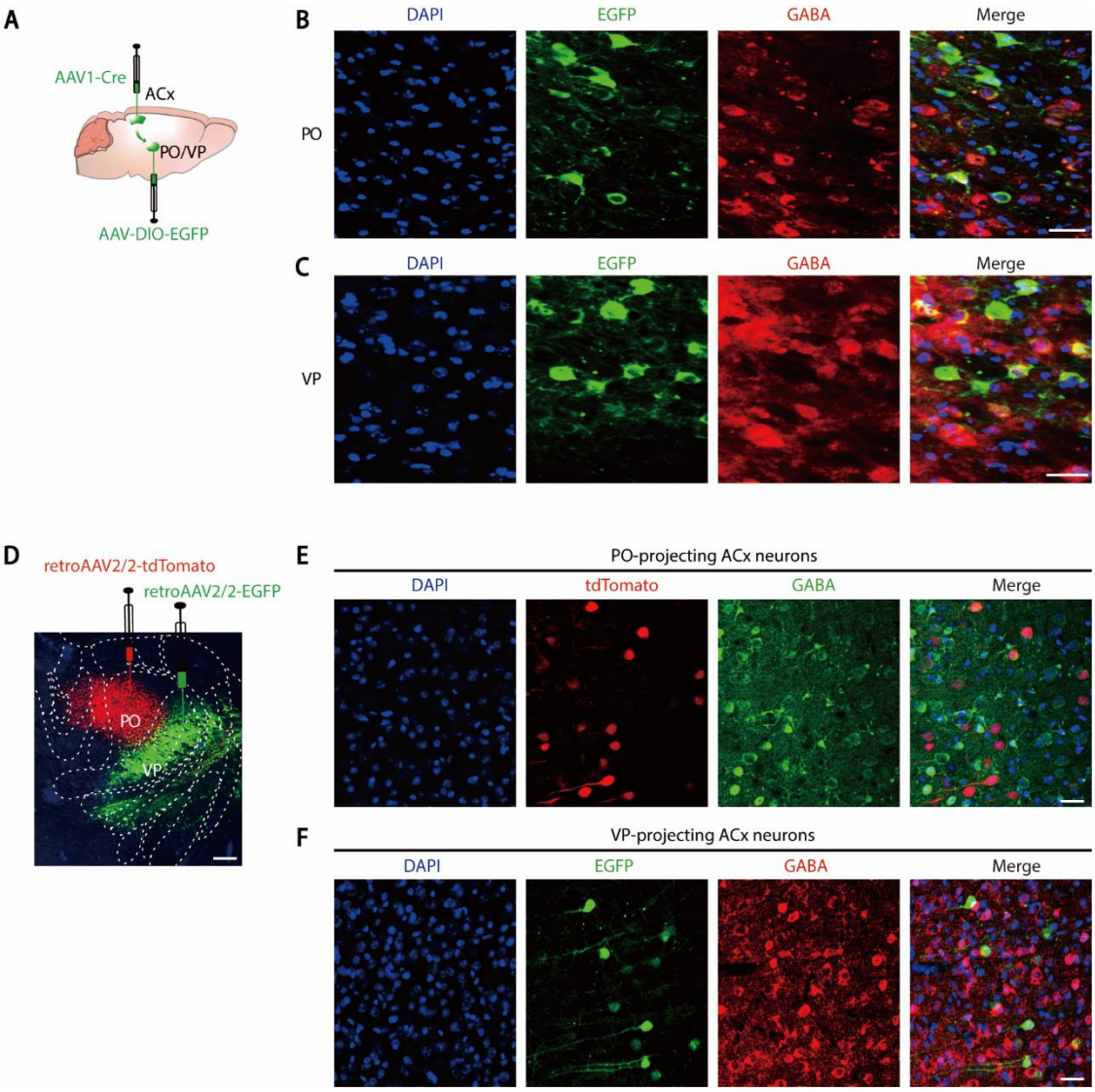
A
AAV1-Cre
ACx
PO/VP
AAV-DIO-EGFP
B
DAPI
EGFP
GABA
Merge
PO
C
DAPI
EGFP
GABA
Merge
VP
D
retroAAV2/2-tdTomato
retroAAV2/2-EGFP
PO
VP
E
PO-projecting ACx neurons
DAPI
tdTomato
GABA
Merge
F
VP-projecting ACx neurons
DAPI
EGFP
GABA
Merge

Fig. S12. Cell type identification in the ACx→PO and ACx→VP circuits.

(**A**) Schematic of viral injection. (**B** and **C**) Representative images showing EGFP-labeled neurons within the PO (B) and VP (C) co-localized with GABA immunofluorescence. Scale bars, 50 μm. (**D**) A representative image showing the viral expression within the PO and VP. Scale bar, 200 μm. (**E** and **F**) Representative images showing tdTomato-labeled (**E**) or EGFP-labeled (**F**) neurons within the ACx co-localized with GABA immunofluorescence. Scale bars, 50 μm.

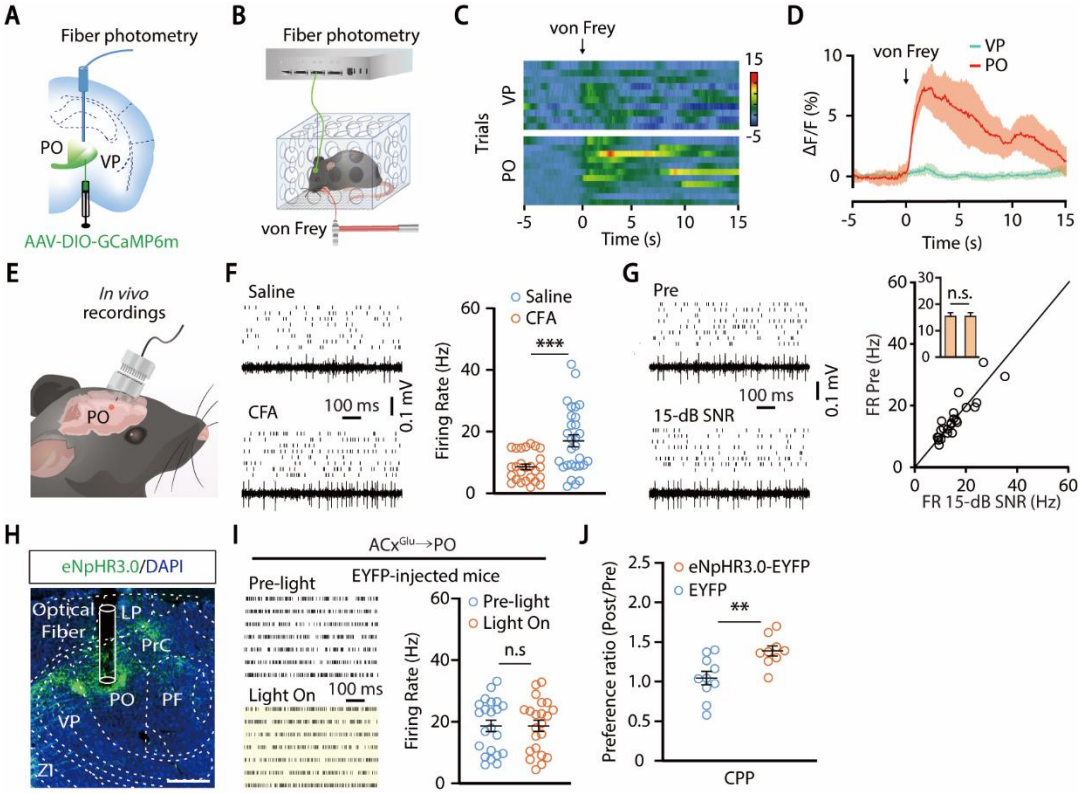
A
Fiber photometry
PO
VP
AAV-DIO-GCaMP6m
B
Fiber photometry
von Frey
C
von Frey
Trials
VP
PO
15
-5
-5
0
5
10
15
Time (s)
D
von Frey
VP
PO
ΔF/F (%)
10
5
0
-5
0
5
10
15
Time (s)
E
In vivo recordings
PO
F
Saline
CFA
100 ms
0.1 mV
Saline
CFA
***
Firing Rate (Hz)
60
40
20
0
G
Pre
15-dB SNR
100 ms
0.1 mV
n.s.
30
20
10
0
FR Pre (Hz)
FR 15-dB SNR (Hz)
0
20
40
60
H
eNpHR3.0/DAPI
Optical Fiber
LP
PrC
PO
PF
VP
ZI
I
ACx^Glu→PO
EYFP-injected mice
Pre-light
Light On
100 ms
Pre-light
Light On
n.s
Firing Rate (Hz)
60
40
20
0
J
eNpHR3.0-EYFP
EYFP
**
Preference ratio (Post/Pre)
2.5
2.0
1.5
1.0
0.5
0
CPP

Fig. S13. Increased activity of PO^{Glu} neurons in CFA mice.

(**A**) Schematic of viral injection for fiber photometry recording. (**B**) Schematic of fiber photometry recording in freely moving mice. (**C** and **D**) Heatmaps (C) and mean data (D) showing that Ca^{2+} signals were rapidly increased by punctate mechanical stimulation (von Frey filament, 0.04 g) of the CFA-treated hindpaw (n = 5 mice for each group). The colored bar in C indicates ΔF/F (%). (**E**) Schematic of multi-tetrode recording in freely moving mice. (**F**) Raster plots and voltage traces of the spontaneous firings recorded in PO neurons from saline and CFA mice (left), and summarized data (right, saline, n = 26 cells from four mice; CFA, n = 29 cells from four mice; t_{53} = 3.771, P = 0.0004). (**G**) Raster plots and voltage traces of spontaneous firings recorded in PO neurons before and during exposure to 15-dB SNR white noise (left), and summarized data of firing rate (right, n = 23 cells from four mice; t_{22} = 0.03488, P = 0.9725). (**H**) A representative image of optical fiber placement in the PO. (**I**) Raster plots of spontaneous firings recorded in PO neurons before and during 594 nm light delivery in the PO of the *CaMKII-Cre* mice with the ACx injection of DIO-EYFP (left), and summarized data (right, n = 22 cells from four mice; t_{21} = 0.02134, P = 0.9832). (**J**) Summarized data for place preference in CFA mice following optical inhibition of the $ACx^{Glu}\rightarrow PO$ circuit (EYFP, n = 10 mice; eNpHR3.0-EYFP, n = 9 mice; t_{17} = 3.151, $P = 0.0058$). The data are expressed as the mean ± s.e.m. $^{**}P < 0.01$; $^{***}P < 0.001$. n.s., not significant. Details of the statistical analyses are presented in table S2.

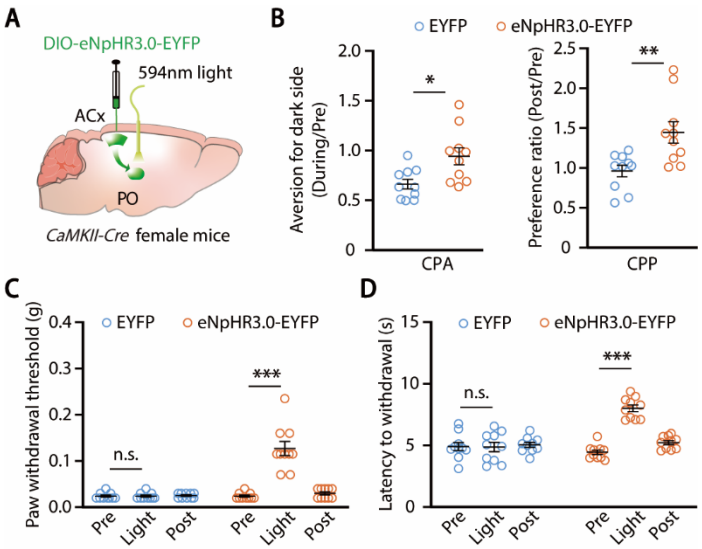
A
DIO-eNpHR3.0-EYFP
594nm light
ACx
PO
CaMKII-Cre female mice
B
EYFP
eNpHR3.0-EYFP
Aversion for dark side (During/Pre)
CPA
Preference ratio (Post/Pre)
CPP
C
Paw withdrawal threshold (g)
n.s.
***
Pre
Light
Post
D
Latency to withdrawal (s)
n.s.
***

Fig. S14. Optical inhibition of the ACx^{Glu}→PO circuit induces analgesia in female CFA mice.

(**A**) Schematic of viral injection for optical manipulation. (**B**) Summarized data for place aversion (left, n = 10 mice each group; t_{18} = 2.825, P = 0.0112) and preference (right, n = 10 mice each group; t_{18} = 3.179, P = 0.0052) following optical inhibition of the ACx^{Glu}→PO circuit in female mice treated with CFA. (**C** and **D**) Summarized data for mechanical (C, n = 10 mice each group; $F_{2,36}$ = 41.26, P < 0.0001) and thermal (D, n = 10 mice each group; $F_{2,36}$ = 42.57, P < 0.0001) nociceptive thresholds following optical inhibition of the ACx^{Glu}→PO circuit in female CFA mice. The data are expressed as the mean ± s.e.m. *P < 0.05; **P < 0.01; ***P < 0.001. n.s., not significant. Details of the statistical analyses are presented in table S2.

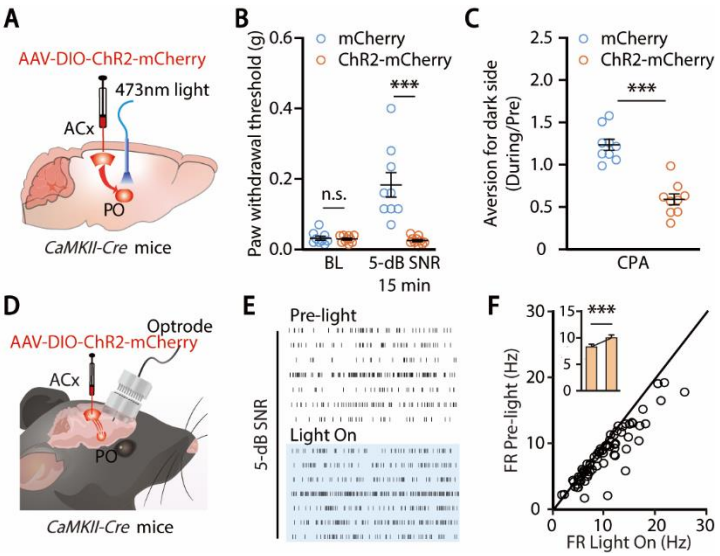
A
AAV-DIO-ChR2-mCherry
473nm light
ACx
PO
CaMKII-Cre mice
B
mCherry
ChR2-mCherry
Paw withdrawal threshold (g)
0.6
0.4
0.2
0.0
***
n.s.
BL
5-dB SNR
15 min
C
mCherry
ChR2-mCherry
Aversion for dark side (During/Pre)
2.5
2.0
1.5
1.0
0.5
0
***
CPA
D
Optrode
AAV-DIO-ChR2-mCherry
ACx
PO
CaMKII-Cre mice
E
Pre-light
5-dB SNR
Light On
F
FR Pre-light (Hz)
30
20
10
0
15
10
5
0
***
0
10
20
30
FR Light On (Hz)

Fig. S15. Effects of optical activation of the ACx^{Glu}→PO circuit on CFA mice exposed to low SNR sound.

(**A**) Schematic for optical activation of the ACx^{Glu}→PO circuit. (**B** and **C**) Summarized data for the mechanical nociceptive threshold (B, mCherry, n = 9 mice; ChR2-mCherry, n = 10 mice; $F_{1,17} = 21.80$, $P = 0.0002$) and place aversion (C, n = 9 mice each group; $t_{16} = 6.971$, $P < 0.0001$) in CFA mice exposed to 5-dB SNR white noise during optical activation of the ACx^{Glu}→PO circuit. (**D**) Schematic of viral injection for *in vivo* multi-tetrode recording during optical activation of the ACx^{Glu}→PO circuit. (**E** and **F**) Raster plots of spontaneous firings recorded in PO neurons before and during optical activation of ACx^{Glu} terminals in the PO of *CaMKII-Cre* mice exposed to 5-dB SNR white noise (E), and summarized data (F, n = 70 cells from seven mice; $t_{69} = 7.072$, $P < 0.0001$). The data are expressed as the mean ± s.e.m. ***$P < 0.001$. n.s., not significant. Details of the statistical analyses are presented in table S2.

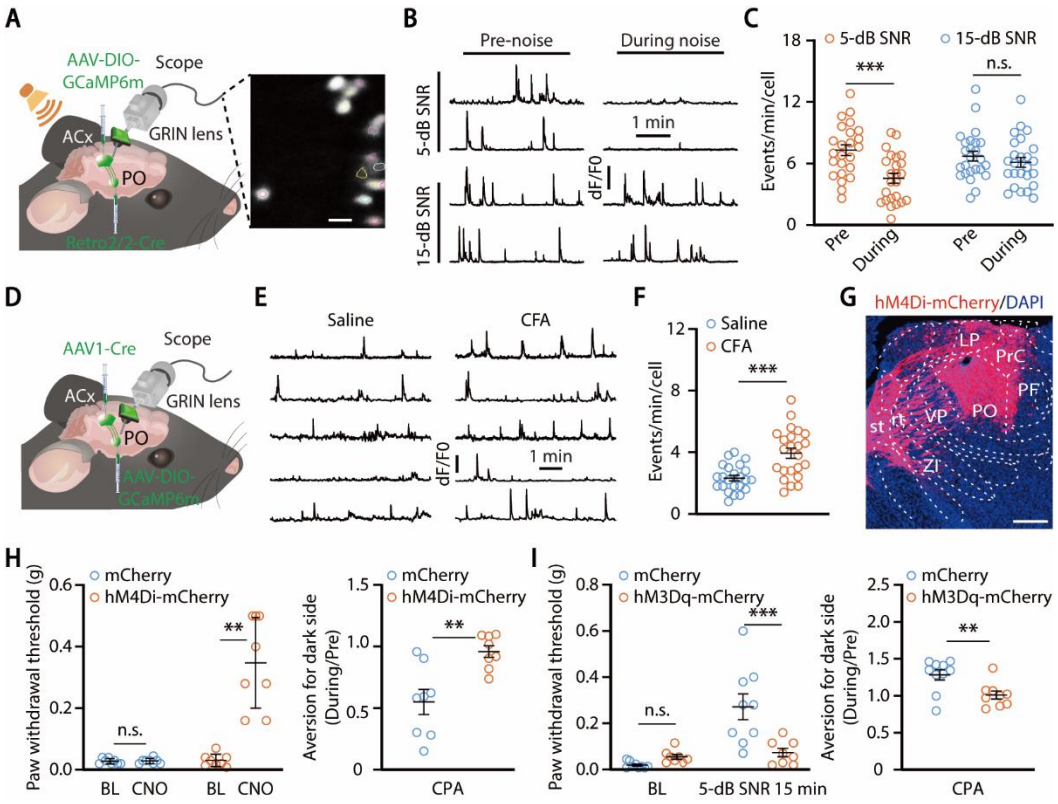
A
AAV-DIO-GCaMP6m
Scope
ACx
GRIN lens
PO
Retro2/2-Cre
B
Pre-noise
During noise
5-dB SNR
15-dB SNR
1 min
dF/F0
C
5-dB SNR
15-dB SNR
Events/min/cell
***
n.s.
Pre
During
D
AAV1-Cre
Scope
ACx
GRIN lens
PO
AAV-DIO-GCaMP6m
E
Saline
CFA
1 min
dF/F0
F
Saline
CFA
Events/min/cell
***
G
hM4Di-mCherry/DAPI
LP
PrC
PF
st
rt
VP
PO
ZI
H
mCherry
hM4Di-mCherry
Paw withdrawal threshold (g)
n.s.
**
BL
CNO
Aversion for dark side (During/Pre)
CPA
I
mCherry
hM3Dq-mCherry
Paw withdrawal threshold (g)
n.s.
***
BL
5-dB SNR 15 min
Aversion for dark side (During/Pre)
CPA

Fig. S16. Inhibition of the PO neurons receiving ACx projections mediates low SNR sound-induced analgesia in inflamed hindpaws.

(**A**) Schematic of vial injections for microendoscopic calcium imaging, and an example field of view in an imaged mouse showing GCaMP6m signals in ACx neurons. Scale bar, 50 μm. (**B** and **C**) Representative traces of the spontaneous Ca^{2+} signals recorded in PO-projecting ACx neurons before and during exposure to 5-dB or 15-dB SNR white noise (B), and summarized data (C, 5-dB SNR, $n = 24$ cells from four mice; 15-dB SNR, $n = 25$ cells from four mice; $F_{1,47} = 15.90$, $P = 0.0002$). (**D**) Schematic of vial injections for microendoscopic calcium imaging of PO neurons receiving ACx projections. (**E** and **F**) Representative traces of the spontaneous Ca^{2+} signals recorded in PO neurons receiving ACx projections in saline and CFA mice (E), and summarized data (F, saline, $n = 21$ cells from four mice; CFA, $n = 23$ cells from four mice; $t_{42} = 11.98$, $P < 0.0001$). (**G**) A representative image of hM4Di-mCherry expression in PO neurons receiving ACx projections. Scale bar, 500 μm. (**H**) The mechanical nociceptive threshold (left, $n = 8$ mice each group; mCherry, BL vs. CNO, $W = 1$, $P > 0.9999$; hM4Di-mCherry, BL vs. CNO, $W = 36$, $P = 0.0078$) and place aversion (right, $n = 8$ mice each group; $t_{14} = 3.601$, $P = 0.0029$) of CFA mice before and during chemogenetic inactivation of PO neurons receiving ACx projections. (**I**) The mechanical nociceptive threshold (left, mCherry, $n = 9$ mice; hM3Dq-mCherry, $n = 8$ mice; $F_{1,15} = 14.47$, $P = 0.0017$) and place aversion (right, mCherry, $n = 10$ mice; hM3Dq-mCherry, $n = 9$ mice; $t_{17} = 3.056$, $P = 0.0072$) of CFA mice exposed to 5-dB SNR white noise before and during chemogenetic inactivation of PO neurons receiving ACx projections. The data are expressed as the mean ± s.e.m. $^{**}P < 0.01$; $^{***}P < 0.001$. n.s., not significant. Details of the statistical analyses are presented in table S2.

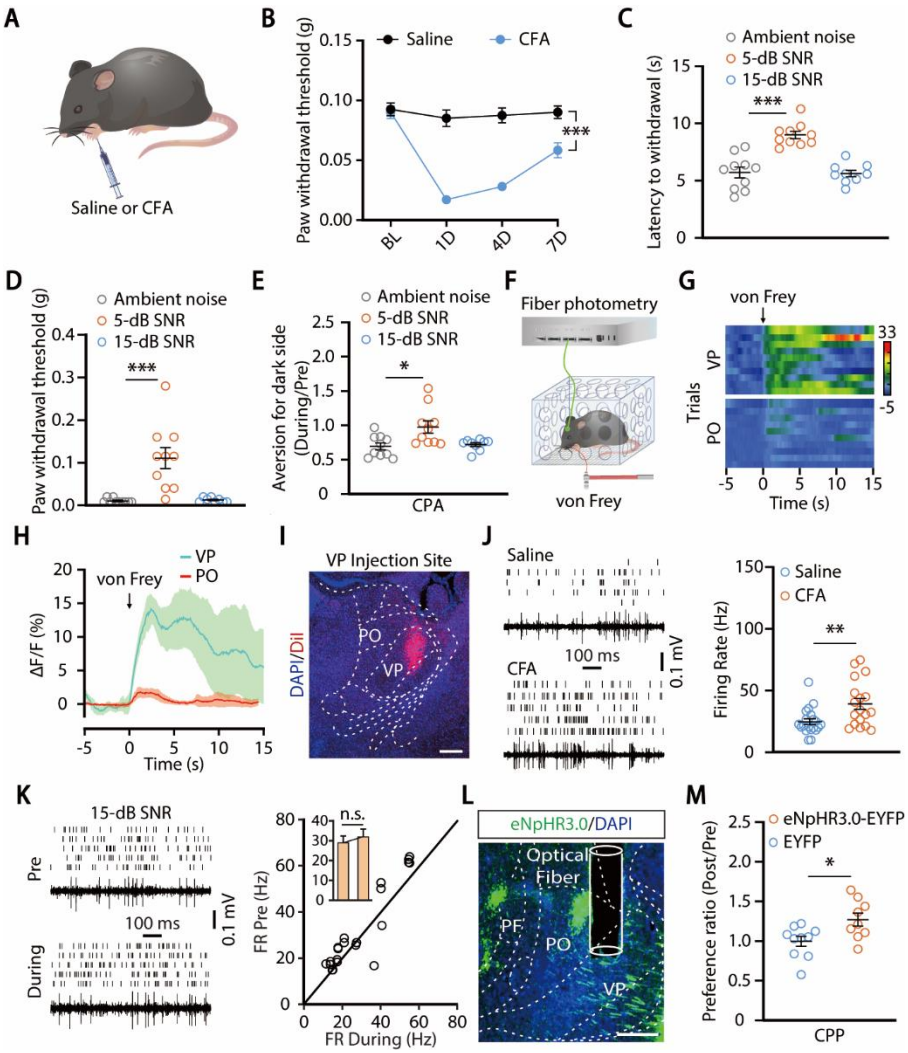
A
Saline or CFA
B
Saline
CFA
Paw withdrawal threshold (g)
0.15
0.10
0.05
0.00
***
BL
1D
4D
7D
C
Ambient noise
5-dB SNR
15-dB SNR
Latency to withdrawal (s)
***
D
Ambient noise
5-dB SNR
15-dB SNR
Paw withdrawal threshold (g)
***
E
Ambient noise
5-dB SNR
15-dB SNR
Aversion for dark side (During/Pre)
*
CPA
F
Fiber photometry
von Frey
G
von Frey
VP
PO
Trials
33
-5
Time (s)
H
VP
PO
von Frey
ΔF/F (%)
Time (s)
I
VP Injection Site
DAPI/DiI
PO
VP
J
Saline
100 ms
0.1 mV
CFA
Saline
CFA
Firing Rate (Hz)
**
K
15-dB SNR
Pre
During
100 ms
0.1 mV
n.s.
FR Pre (Hz)
FR During (Hz)
L
eNpHR3.0/DAPI
Optical Fiber
PF
PO
VP
M
eNpHR3.0-EYFP
EYFP
Preference ratio (Post/Pre)
*
CPP

Fig. S17. Increased activity of VP neurons receiving ACx projections in mice with forepaw inflammatory pain.

(**A**) Schematic for inducing forepaw inflammation. (**B**) The mechanical nociceptive threshold of inflamed forepaws based on the von Frey test (n = 9 mice each group; $F_{3,48} = 30.28$, $P < 0.0001$). (**C** to **E**) Summarized data for thermal (C, ambient noise, n = 10 mice; 5-dB SNR, n = 10 mice; 15-dB SNR, n = 9 mice; $F_{2,26} = 27.04$, $P < 0.0001$), mechanical nociceptive thresholds (D, ambient noise, n = 10 mice; 5-dB SNR, n = 10 mice; 15-dB SNR, n = 8 mice; $F_{2,25} = 14.49$, $P < 0.0001$), and place aversion (E, ambient noise, n = 10 mice; 5-dB SNR, n = 10 mice; 15-dB SNR, n = 9 mice; $F_{2,26} = 6.197$, $P = 0.0063$) of CFA mice exposed to different SNR white noise. (**F**) Schematic of fiber photometry recording in freely moving mice with punctate mechanical stimulation (von Frey filament, 0.02 g) of the CFA-injected forepaw. (**G** and **H**) The heatmaps (G) and mean data (H) showing the Ca^{2+} signals of PO^{Glu} and VP^{Glu} neurons. The colored bar in G indicates ΔF/F (%). (**I**) A representative image showing DiI-labelled recording sites of the tetrode electrodes. Scale bar, 200 μm. (**J**) Raster plots and the typical voltage traces of spontaneous firings recorded in VP neurons from the indicated mice (left), and summarized data (right, Saline, n = 20 cells from three mice; CFA, n = 18 cells from three mice; $t_{36} = 2.98$, $P = 0.0051$). (**K**) Raster plots and typical voltage traces of spontaneous firings recorded in VP neurons from mice with forepaw inflammation before and during exposure to 15-dB SNR white noise (left), and summarized data (right, n = 21 cells from three mice; $t_{20} = 2.049$, $P = 0.0538$). (**L**) A representative image of the optical fiber placement. (**M**) Summarized data of the preference for light-delivery side in the CPP test following optical inhibition of the ACx^{Glu}→PO circuit in CFA mice (EYFP, n = 10 mice; eNpHR3.0-EYFP, n = 9 mice; t_{17} = 2.689, $P = 0.0155$). The data are expressed as the mean ± s.e.m. $^{*}P < 0.05$; $^{**}P < 0.01$; $^{***}P < 0.001$. n.s., not significant. Details of the statistical analyses are presented in table S2.

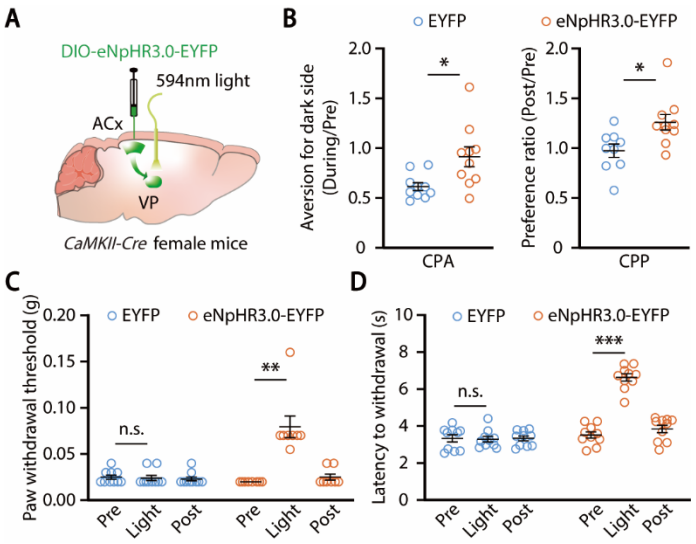
A
DIO-eNpHR3.0-EYFP
594nm light
ACx
VP
CaMKII-Cre female mice
B
EYFP
eNpHR3.0-EYFP
Aversion for dark side (During/Pre)
Preference ratio (Post/Pre)
CPA
CPP
C
Paw withdrawal threshold (g)
n.s.
**
Pre
Light
Post
D
Latency to withdrawal (s)
***

Fig. S18. Optical inhibition of the ACx^{Glu}→VP circuit induces analgesia in female mice with forepaw inflammatory pain.

(**A**) Schematic of viral injection for optical inhibition of the ACx^{Glu}→VP circuit in female mice. (**B**) Summarized data for place aversion (left, n = 10 mice each group; t_{18} = 2.778, P = 0.0155) and preference (right, EYFP, n = 9 mice; eNpHR3.0-EYFP, n = 10 mice; t_{17} = 2.736, P = 0.0124) following optical inhibition of the ACx^{Glu}→VP circuit in female mice with forepaw inflammation. (**C** and **D**) Summarized data for mechanical (C, EYFP, n = 9 mice; eNpHR3.0-EYFP, n = 8 mice; $F_{2,32}$ = 23.58, P < 0.0001) and thermal (D, n = 10 mice each group; $F_{2,36}$ = 76.64, P < 0.0001) nociceptive thresholds following optical inhibition of the ACx^{Glu}→VP circuit in female mice with forepaw inflammation. The data are expressed as the mean ± s.e.m. *P < 0.05; **P < 0.01; ***P < 0.001. n.s., not significant. Details of the statistical analyses are presented in table S2.

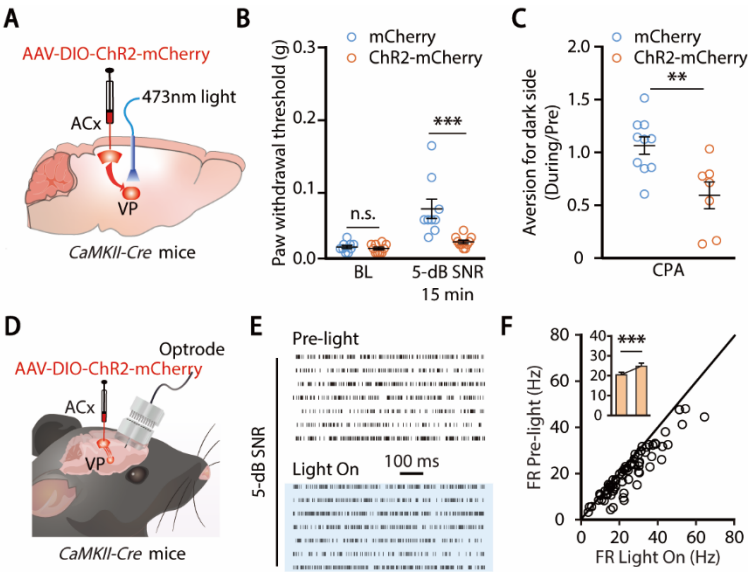
A
AAV-DIO-ChR2-mCherry
473nm light
ACx
VP
CaMKII-Cre mice
B
mCherry
ChR2-mCherry
Paw withdrawal threshold (g)
0.3
0.2
0.1
0.0
***
n.s.
BL
5-dB SNR
15 min
C
mCherry
ChR2-mCherry
**
Aversion for dark side (During/Pre)
2.0
1.5
1.0
0.5
0
CPA
D
Optrode
AAV-DIO-ChR2-mCherry
ACx
VP
CaMKII-Cre mice
E
Pre-light
5-dB SNR
Light On
100 ms
F
***
FR Pre-light (Hz)
80
60
40
20
0
0 20 40 60 80
FR Light On (Hz)

Fig. S19. Behavioral effects of optical activation of the ACx^{Glu}→VP circuit on CFA mice exposed to low SNR sound.

(**A**) Schematic of optogenetic activation of the ACx^{Glu}→VP circuit. (**B** and **C**) Summarized data for the mechanical nociceptive threshold (B, mCherry, n = 9 mice; ChR2-mCherry, n = 10 mice; $F_{1,17} = 9.291$, $P = 0.0073$) and place aversion (C, mCherry, n = 10 mice; ChR2-mCherry, n = 7 mice; $t_{15} = 3.246$, $P = 0.0054$) in mice with forepaw inflammation exposed to 5-dB SNR white noise during optical activation of the ACx^{Glu}→VP circuit. (**D**) Schematic of *in vivo* multi-tetrode recording during optical activation of the ACx^{Glu}→VP circuit. (**E** and **F**) Raster plots of spontaneous firings recorded in VP neurons before and during optical activation of ACx^{Glu} terminals in the VP of *CaMKII-Cre* mice exposed to 5-dB SNR white noise (E), and summarized data (F, n = 72 cells from seven mice; $t_{71} = 7.759$, $P < 0.0001$). The data are expressed as the mean ± s.e.m. $^{**}P < 0.01$; $^{***}P < 0.001$. n.s., not significant. Details of the statistical analyses are presented in table S2.

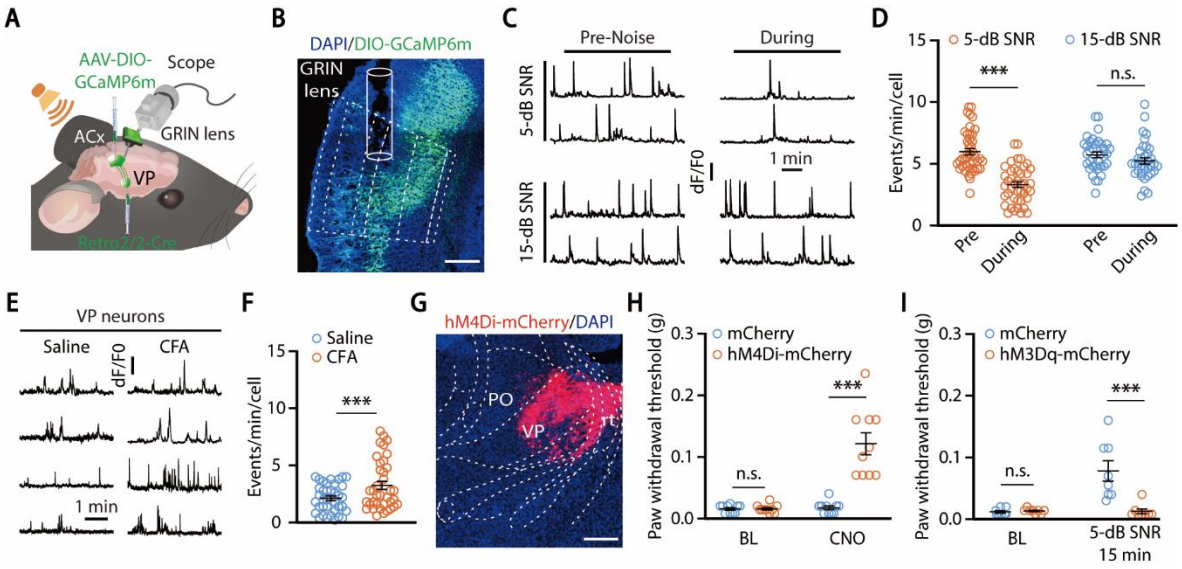
A
AAV-DIO-GCaMP6m
Scope
ACx
GRIN lens
VP
Retro2/2-Cre
B
DAPI/DIO-GCaMP6m
GRIN lens
C
Pre-Noise
During
5-dB SNR
15-dB SNR
dF/F0
1 min
D
5-dB SNR
15-dB SNR
Events/min/cell
***
n.s.
Pre
During
E
VP neurons
Saline
CFA
dF/F0
1 min
F
Saline
CFA
Events/min/cell
***
G
hM4Di-mCherry/DAPI
PO
VP
H
mCherry
hM4Di-mCherry
Paw withdrawal threshold (g)
n.s.
***
BL
CNO
I
mCherry
hM3Dq-mCherry
Paw withdrawal threshold (g)
n.s.
***
BL
5-dB SNR
15 min

Fig. S20. Inhibition of the VP neurons receiving ACx projections mediates low SNR sound-induced increase in forepaw nociceptive threshold.

(**A**) Schematic of vial injections for microendoscopic calcium imaging. (**B**) A representative image showing GCaMP6m fluorescence and the track of lens in the ACx. Scale bar, 200 μm. (**C** and **D**) Representative traces of the spontaneous Ca^{2+} signals recorded in VP-projecting ACx neurons before and during exposed to 5-dB or 15-dB SNR white noise (C), and summarized data (D, 5-dB SNR, n = 43 cells from five mice; 15-dB SNR, n = 36 cells from five mice; $F_{1,77} = 25.17$, $P < 0.0001$). (**E** and **F**) Representative traces of the spontaneous Ca^{2+} signals recorded in VP neurons receiving ACx projections in Saline- and CFA-treated mice (E), and summarized data (F, n = 37 cells from five mice each group; t_{72} = 2.739, $P < 0.0001$). (**G**) A representative image of hM4Di-mCherry expression in VP neurons receiving ACx projections. Scale bar, 500 μm. (**H**) The mechanical nociceptive threshold of the inflamed forepaws before (BL) and during chemogenetic inhibition (CNO) of VP neurons receiving ACx projections (n = 10 mice each group; BL, mCherry vs. hM4Di-mCherry at BL, U = 47, P = 0.8208; mCherry vs. hM4Di-mCherry at CNO, U = 0, P <0.0001). (**I**) The mechanical nociceptive threshold of the inflamed forepaws following chemogenetic activation of VP neurons receiving ACx projections in mice exposed to 5-dB SNR white noise (n = 8 mice each group; mCherry vs. hM3Dq-mCherry at BL, U = 24.5, P = 0.3930; mCherry vs. hM3Dq-mCherry at CNO, U = 2, P = 0.0006). The data are expressed as the mean ± s.e.m. $^{**}P < 0.01$; $^{***}P < 0.001$. n.s., not significant. Details of the statistical analyses are presented in table S2.

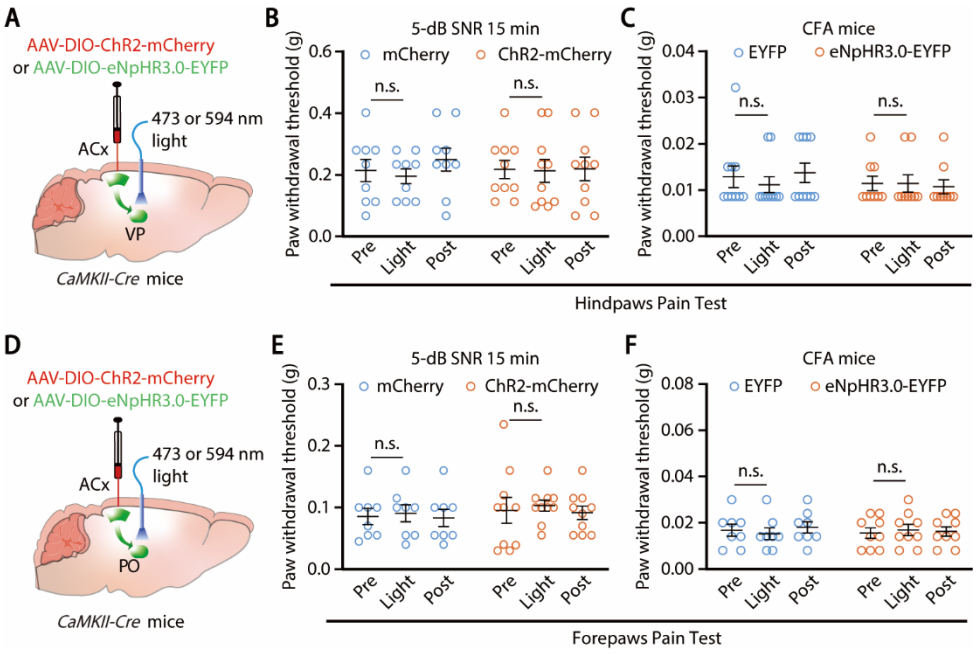
A
AAV-DIO-ChR2-mCherry
or AAV-DIO-eNpHR3.0-EYFP
473 or 594 nm
light
ACx
VP
CaMKII-Cre mice
B
5-dB SNR 15 min
mCherry
ChR2-mCherry
Paw withdrawal threshold (g)
n.s.
Pre
Light
Post
C
CFA mice
EYFP
eNpHR3.0-EYFP
Hindpaws Pain Test
D
AAV-DIO-ChR2-mCherry
or AAV-DIO-eNpHR3.0-EYFP
473 or 594 nm
light
ACx
PO
CaMKII-Cre mice
E
5-dB SNR 15 min
F
CFA mice
Forepaws Pain Test

Fig. S21. Effects of optical manipulation of the ACx^{Glu}→PO and ACx^{Glu}→VP circuits on nociceptive thresholds.

(**A**) Schematic for optical manipulation of the ACx^{Glu}→VP circuit. (**B** and **C**) The mechanical nociceptive threshold of inflamed hindpaws following optical activation (B, mCherry, $n = 9$ mice; ChR2-mCherry, $n = 10$ mice; $F_{2,34} = 0.231$, $P = 0.795$) or inhibition (C, EYFP, $n = 10$ mice; eNpHR3.0-EYFP, $n = 9$ mice; $F_{2,34} = 0.9613$, $P = 0.3925$) of the ACx^{Glu}→VP circuit. (**D**) Schematic for optical manipulation of the ACx^{Glu}→PO circuit. (**E** and **F**) The mechanical nociceptive threshold of inflamed forepaws following optical activation (E, mCherry, $n = 8$ mice; ChR2-mCherry, $n = 10$ mice; $F_{2,32} = 0.011$, $P = 0.9891$) or inhibition (F, EYFP, $n = 8$ mice; eNpHR3.0-EYFP, $n = 9$ mice; $F_{2,30} = 0.316$, $P = 0.7314$) of the ACx^{Glu}→PO circuit. The data are expressed as the mean ± s.e.m. n.s., not significant. Details of the statistical analyses are presented in table S2.

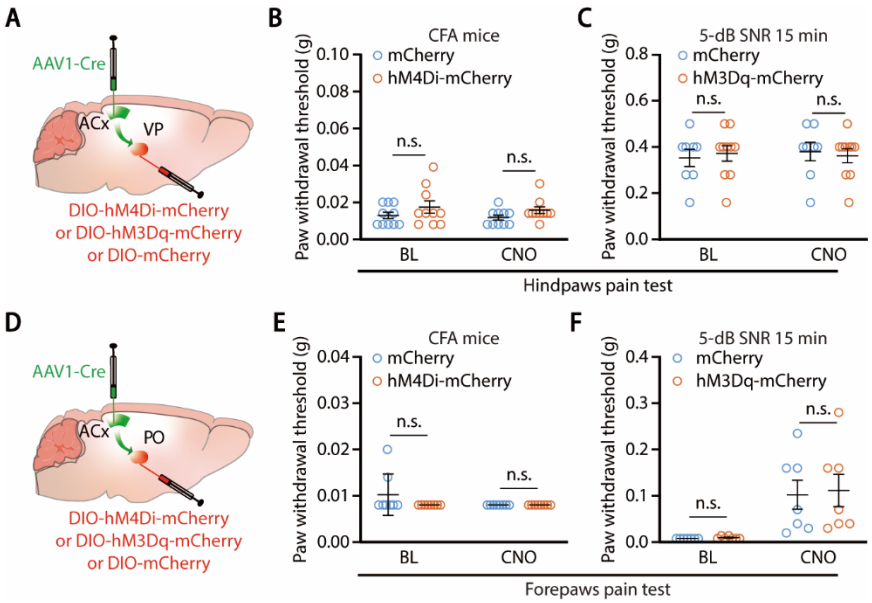
A
AAV1-Cre
ACx
VP
DIO-hM4Di-mCherry
or DIO-hM3Dq-mCherry
or DIO-mCherry
B
CFA mice
mCherry
hM4Di-mCherry
Paw withdrawal threshold (g)
0.10
0.08
0.06
0.04
0.02
0.00
n.s.
n.s.
BL
CNO
C
5-dB SNR 15 min
mCherry
hM3Dq-mCherry
0.8
0.6
0.4
0.2
0.0
n.s.
n.s.
BL
CNO
Hindpaws pain test
D
AAV1-Cre
ACx
PO
DIO-hM4Di-mCherry
or DIO-hM3Dq-mCherry
or DIO-mCherry
E
CFA mice
mCherry
hM4Di-mCherry
Paw withdrawal threshold (g)
0.04
0.03
0.02
0.01
0.00
n.s.
n.s.
BL
CNO
F
5-dB SNR 15 min
mCherry
hM3Dq-mCherry
0.4
0.3
0.2
0.1
0.0
n.s.
n.s.
BL
CNO
Forepaws pain test

Fig. S22. Effects of chemogenetic manipulation of VP or PO neurons receiving ACx projections on nociceptive thresholds.

(**A**) Schematic for chemegenetic activation or inhibition of VP neurons receiving ACx projections. (**B** and **C**) The mechanical nociceptive threshold of inflamed hindpaws before and during inhibition of VP neurons receiving ACx projections (B, n = 10 mice each group; $F_{1,18} = 0.01384$, $P = 0.9077$), or activation of these neurons in mice exposed to 5-dB SNR white noise (C, mCherry, n = 8 mice; hM3Dq-mCherry, n = 10 mice; $F_{1,16} = 0.6504$, $P = 0.4318$). (**D**) Schematic for chemogenetic activation or inhibition of PO neurons receiving ACx projections. (**E** and **F**) The mechanical nociceptive threshold of the CFA-injected forepaws before and during inhibition of the PO neurons receiving ACx projections (E, n = 8 mice each group; mCherry vs. hM4Di-mCherry at BL, U = 24, P = 0.4667; mCherry vs. hM4Di-mCherry at CNO, U = 32, $P > 0.9999$), or activation of these neurons in mice exposed to 5-dB SNR white noise (F, n = 7 mice each group; mCherry vs. hM3Dq-mCherry at BL, U = 17.5, P = 0.4615; mCherry vs. hM3Dq-mCherry at CNO, U = 22, P = 0.7855). The data are expressed as the mean ± s.e.m. n.s., not significant. Details of the statistical analyses are presented in table S2.

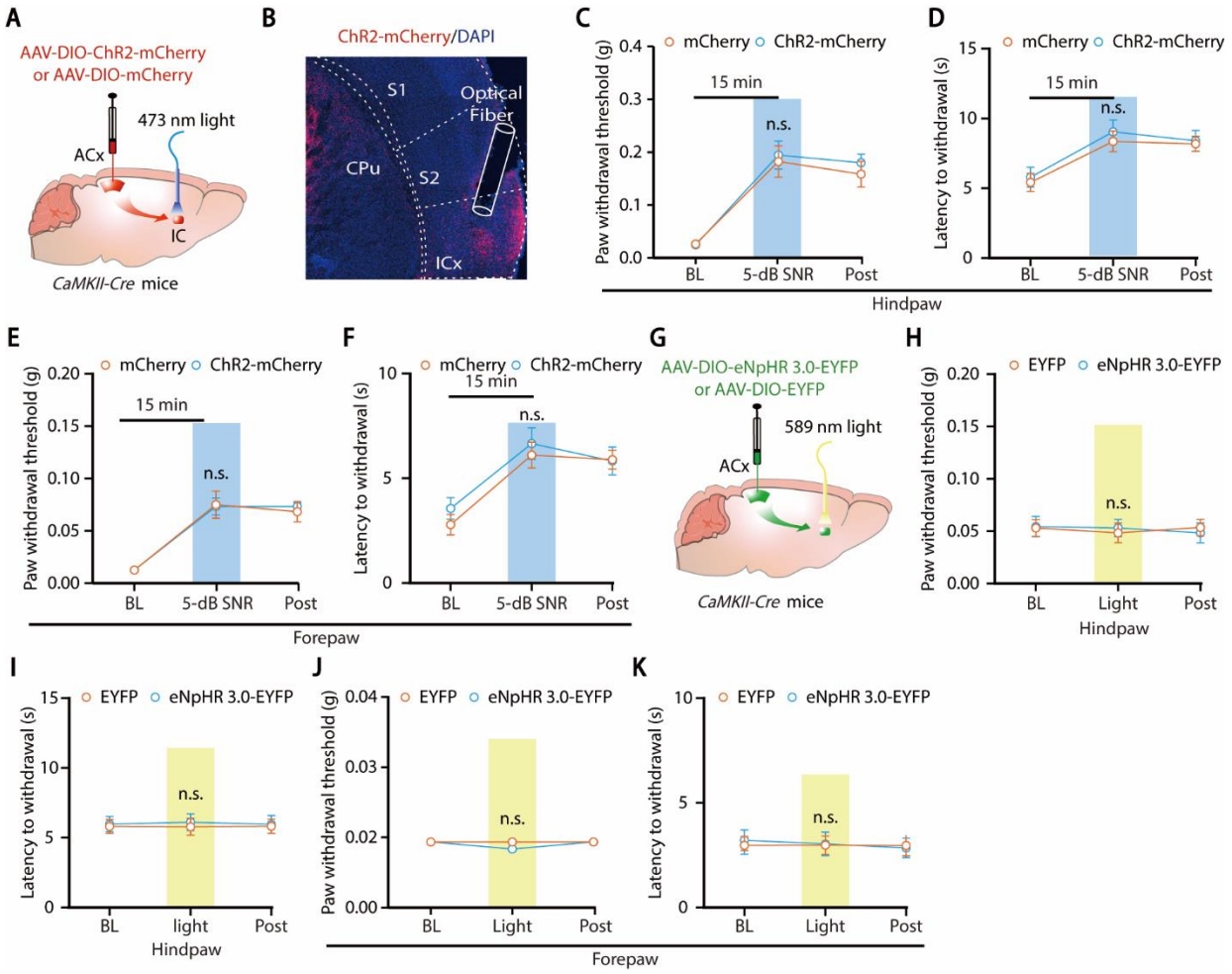
A
AAV-DIO-ChR2-mCherry
or AAV-DIO-mCherry
473 nm light
ACx
IC
CaMKII-Cre mice
B
ChR2-mCherry/DAPI
S1
Optical
Fiber
CPu
S2
ICx
C
mCherry ChR2-mCherry
15 min
n.s.
Paw withdrawal threshold (g)
BL
5-dB SNR
Post
Hindpaw
D
mCherry ChR2-mCherry
15 min
n.s.
Latency to withdrawal (s)
BL
5-dB SNR
Post
E
mCherry ChR2-mCherry
15 min
n.s.
Paw withdrawal threshold (g)
BL
5-dB SNR
Post
Forepaw
F
mCherry ChR2-mCherry
15 min
n.s.
Latency to withdrawal (s)
BL
5-dB SNR
Post
G
AAV-DIO-eNpHR 3.0-EYFP
or AAV-DIO-EYFP
589 nm light
ACx
CaMKII-Cre mice
H
EYFP eNpHR 3.0-EYFP
n.s.
Paw withdrawal threshold (g)
BL
Light
Post
Hindpaw
I
EYFP eNpHR 3.0-EYFP
n.s.
Latency to withdrawal (s)
BL
light
Post
Hindpaw
J
EYFP eNpHR 3.0-EYFP
n.s.
Paw withdrawal threshold (g)
BL
Light
Post
K
EYFP eNpHR 3.0-EYFP
n.s.
Latency to withdrawal (s)
BL
Light
Post
Forepaw

Fig. S23. Effects of optical manipulation of the ACx^{Glu}→ICx circuit on nociceptive thresholds in CFA mice.

(**A**) Schematic for optogenetic activation of the ACx^{Glu}→ICx circuit. (**B**) A representative image of the optical fiber placement in the ICx. Scale bar, 200 μm. (**C** and **D**) Mechanical (C, n = 9 mice each group; $F_{2,32} = 0.7963$, $P = 0.2295$) and thermal (D, n = 9 mice each group; $F_{2,32} = 0.9439$, $P = 0.0578$) nociceptive thresholds of inflamed hindpaws in mice exposed to 5-dB SNR white noise upon optical activation of the ACx^{Glu}→ICx circuit. (**E** and **F**) Mechanical (E, n = 9 mice each group; $F_{2,32} = 0.8559$, $P = 0.1563$) and thermal (F, n = 9 mice each group; $F_{2,32} = 0.9037$, $P = 0.4152$) nociceptive thresholds of inflamed forepaws in mice exposed to 5-dB SNR white noise upon optical activation of the ACx^{Glu}→ICx circuit. (**G**) Schematic for optogenetic inhibition of the ACx^{Glu}→ICx circuit. (**H** and **I**) Mechanical (H, n = 10 mice each group; $F_{2,36} = 0.1541$, $P = 0.8578$) and thermal (I, n = 10 mice each group; $F_{2,36} = 0.0292$, $P = 0.9713$) nociceptive thresholds of inflamed hindpaws following optical inhibition of the ACx^{Glu}→ICx circuit. (**J** and **K**) Mechanical (J, n = 10 mice each group; $F_{2,36} = 0.375$, $P = 0.6899$) and thermal (K, n = 10 mice each group; $F_{2,36} = 0.9169$, $P = 0.08698$) nociceptive thresholds of inflamed forepaws following optical inhibition of the ACx^{Glu}→ICx circuit. The data are expressed as the mean ± s.e.m. n.s., not significant. Details of the statistical analyses are presented in table S2.

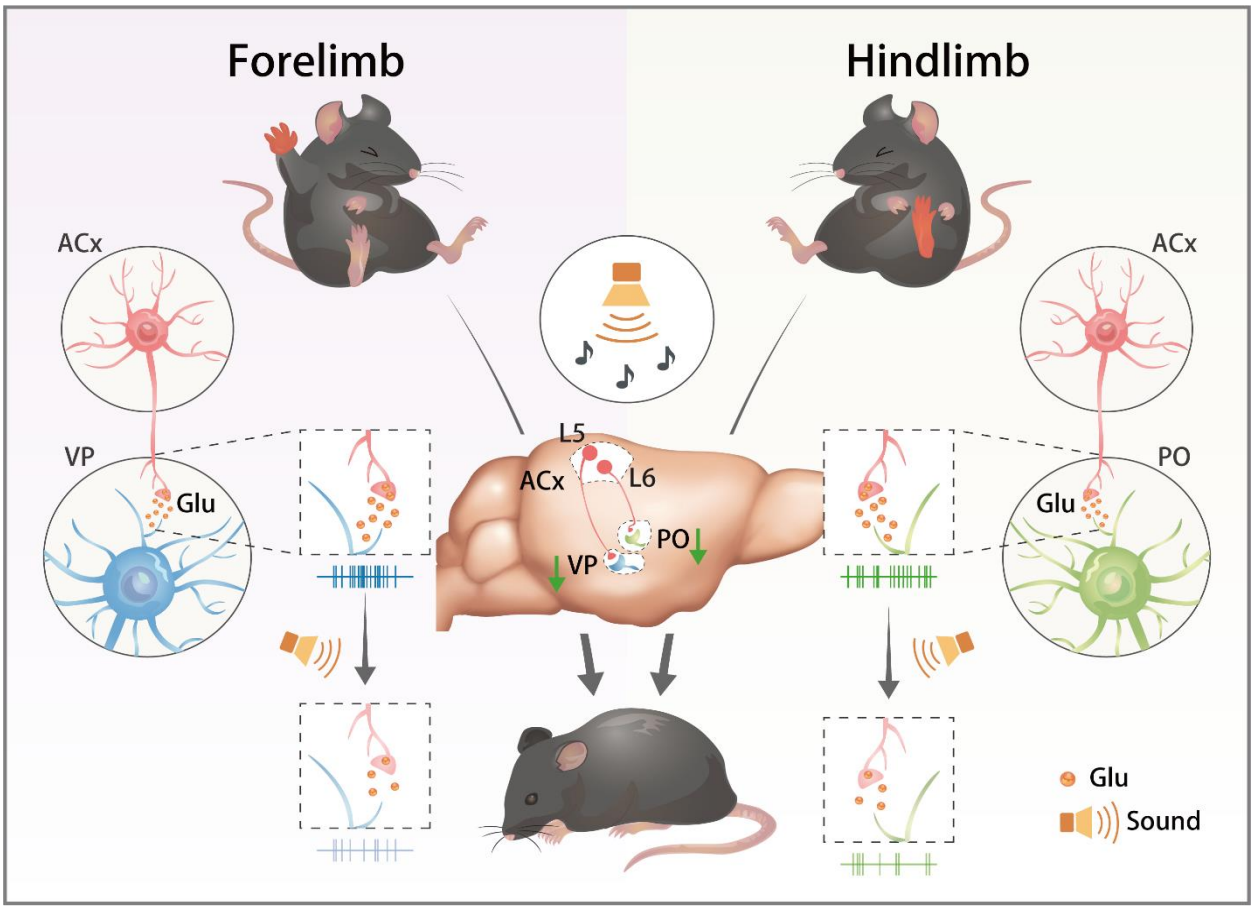

Fig. S24. Inhibition of auditory cortex inputs to the somatosensory thalamus drives sound-induced analgesia.

Inflammatory pain in the hind or forepaws in mice increases the neuronal activity in the thalamic posterior (PO) and ventral posterior (VP) nuclei, respectively. Moreover, low SNR sound (music or noise) treatment inhibits the excitatory projections from the auditory cortex (ACx) to the PO and VP, which lowers the excitability of PO and VP neurons and consequently alleviates the pain hypersensitivity in the inflamed hind and forepaws. Glu, glutamate.

Table S1. Extended statistical information for Figure 1 to Figure 4.

Figure Panel	n/group	Primary statistic	*Post-hoc* test	Comparison	p value	F/t statistic
Fig. 1B	Ambient noise, n = 10 mice 50 dB SPL CS, n = 10 mice 60 dB SPL CS, n = 8 mice	Two-way RM ANOVA	Bonferroni's multiple comparison	Group × time interaction	<0.0001	F(18,250) = 8.783
				Ambient noise vs. 50 dB at BL	>0.9999	
				Ambient noise vs. 50 dB at 10 min	0.0022	
				Ambient noise vs. 50 dB at 20 min	<0.0001	
				Ambient noise vs. 50 dB at 30 min	0.001	
				Ambient noise vs. 50 dB at 40 min	0.9894	
				Ambient noise vs. 50 dB at 50 min	0.9965	
				Ambient noise vs. 50 dB at 24 H	0.9991	
				Ambient noise vs. 50 dB at 48 H	<0.0001	
				Ambient noise vs. 50 dB at 72 H	<0.0001	
				Ambient noise vs. 50 dB at 96 H	<0.0001	
				Ambient noise vs. 60 dB at BL	0.9559	
				Ambient noise vs. 60 dB at 10 min	0.9423	
				Ambient noise vs. 60 dB at 20 min	0.9768	
				Ambient noise vs. 60 dB at 30 min	0.9798	
				Ambient noise vs. 60 dB at 40 min	0.9969	
				Ambient noise vs. 60 dB at 50 min	0.9844	
				Ambient noise vs. 60 dB at 24 H	0.9677	
				Ambient noise vs. 60 dB at 48 H	0.9253	
				Ambient noise vs. 60 dB at 72 H	0.918	
				Ambient noise vs. 60 dB at 96 H	0.5251	
Fig. 1C	Ambient noise, n = 10 mice 50 dB SPL DS, n = 10 mice 60 dB SPL DS, n = 10 mice	Two-way RM ANOVA	Bonferroni's multiple comparison	Group × time interaction	<0.0001	F(18,270) = 8.217
				Ambient noise vs. 50 dB at BL	0.9602	
				Ambient noise vs. 50 dB at 10 min	0.0092	
				Ambient noise vs. 50 dB at 20 min	<0.0001	
				Ambient noise vs. 50 dB at 30 min	<0.0001	
				Ambient noise vs. 50 dB at 40 min	0.6551	
				Ambient noise vs. 50 dB at 50 min	0.999	
				Ambient noise vs. 50 dB at 24 H	0.994	
				Ambient noise vs. 50 dB at 48 H	0.0003	
				Ambient noise vs. 50 dB at 72 H	<0.0001	
				Ambient noise vs. 50 dB at 96 H	0.0004	
				Ambient noise vs. 60 dB at BL	0.9473	
				Ambient noise vs. 60 dB at 10 min	0.77	
				Ambient noise vs. 60 dB at 20 min	0.9962	
				Ambient noise vs. 60 dB at 30 min	0.8902	
				Ambient noise vs. 60 dB at 40 min	0.9083	
				Ambient noise vs. 60 dB at 50 min	0.9978	
				Ambient noise vs. 60 dB at 24 H	0.9251	
				Ambient noise vs. 60 dB at 48 H	0.3876	
				Ambient noise vs. 60 dB at 72 H	0.9914	
				Ambient noise vs. 60 dB at 96 H	0.2102	
Fig. 1D	Ambient noise, n = 10 mice 50 dB SPL WN, n = 10 mice 60 dB SPL WN, n = 8 mice	Two-way RM ANOVA	Bonferroni's multiple comparison	Group × time interaction	<0.0001	F(18,225) = 9.468
				Ambient noise vs. 50 dB at BL	0.3241	
				Ambient noise vs. 50 dB at 10 min	0.0173	
				Ambient noise vs. 50 dB at 20 min	0.0002	
				Ambient noise vs. 50 dB at 30 min	0.0015	
				Ambient noise vs. 50 dB at 40 min	>0.9999	
				Ambient noise vs. 50 dB at 50 min	0.6224	
				Ambient noise vs. 50 dB at 24 H	0.5643	
				Ambient noise vs. 50 dB at 48 H	0.0346	
				Ambient noise vs. 50 dB at 72 H	0.0049	
				Ambient noise vs. 50 dB at 96 H	0.0145	
				Ambient noise vs. 60 dB at BL	>0.9999	
				Ambient noise vs. 60 dB at 10 min	>0.9999	
				Ambient noise vs. 60 dB at 20 min	0.9451	
				Ambient noise vs. 60 dB at 30 min	>0.9999	
				Ambient noise vs. 60 dB at 40 min	>0.9999	
				Ambient noise vs. 60 dB at 50 min	0.7188	
				Ambient noise vs. 60 dB at 24 H	>0.9999	
				Ambient noise vs. 60 dB at 48 H	>0.9999	
				Ambient noise vs. 60 dB at 72 H	0.3647	
				Ambient noise vs. 60 dB at 96 H	0.1417	
Fig. 1E	62 dB SPL, n = 10 mice 67 dB SPL, n = 10 mice 72 dB SPL, n = 8 mice 77 dB SPL, n = 10 mice	Two-way RM ANOVA	Bonferroni's multiple comparison	Group × time interaction	<0.0001	F(3,34) = 28.46
				62 dB SPL Pre vs. During	<0.0001	
				67 dB SPL Pre vs. During	0.086	
				72 dB SPL Pre vs. During	>0.9999	
				77 dB SPL Pre vs. During	>0.9999	
Fig. 1F	Ambient noise, n = 10 mice 5-dB SNR, n = 10 mice 15-dB SNR, n = 10 mice	Two-way RM ANOVA	Bonferroni's multiple comparison	Group × time interaction	< 0.0001	F(18,243) = 3.280
				Ambient noise vs. 5-dB SNR at BL	>0.9999	
				Ambient noise vs. 5-dB SNR at 10 min	0.0504	
				Ambient noise vs. 5-dB SNR at 20 min	<0.0001	

Table S1. Extended statistical information for Figure 1 to Figure 4.

Figure Panel	n/group	Primary statistic	*Post-hoc* test	Comparison	p value	F/t statistic
				Ambient noise vs. 5-dB SNR at 30 min	0.004	
				Ambient noise vs. 5-dB SNR at 40 min	>0.9999	
				Ambient noise vs. 5-dB SNR at 50 min	>0.9999	
				Ambient noise vs. 5-dB SNR at 24 H	>0.9999	
				Ambient noise vs. 5-dB SNR at 48 H	0.0175	
				Ambient noise vs. 5-dB SNR at 72 H	0.0008	
				Ambient noise vs. 5-dB SNR at 96 H	0.0564	
				Ambient noise vs. 15-dB SNR at BL	>0.9999	
				Ambient noise vs. 15-dB SNR at 10 min	0.6962	
				Ambient noise vs. 15-dB SNR at 20 min	>0.9999	
				Ambient noise vs. 15-dB SNR at 30 min	>0.9999	
				Ambient noise vs. 15-dB SNR at 40 min	>0.9999	
				Ambient noise vs. 15-dB SNR at 50 min	0.8048	
				Ambient noise vs. 15-dB SNR at 24 H	0.8124	
				Ambient noise vs. 15-dB SNR at 48 H	0.5388	
				Ambient noise vs. 15-dB SNR at 72 H	>0.9999	
				Ambient noise vs. 15-dB SNR at 96 H	0.5295	
Fig. 1H	Ambient noise, n = 9 mice	One-way ANOVA	Bonferroni's multiple comparison	Main effect of group	0.0165	F(2,26) = 4.828
	50 dB SPL WN, n = 9 mice			Ambient noise vs. 50 dB SPL	0.0136	
	60 dB SPL WN, n = 11 mice			Ambient noise vs. 60 dB SPL	0.3953	
Fig. 1J	Ambient noise, n = 11	One-way ANOVA	Bonferroni's multiple comparison	Main effect of group	0.0015	F(2,26) = 8.384
	5-dB SNR, n = 10			Ambient noise vs. 5-dB SNR	0.0065	
	15-dB SNR, n = 8			Ambient noise vs. 15-dB SNR	>0.9999	
Fig. 2C	5-dB SNR, n = 25 cells from four mice	Two-way RM ANOVA	Bonferroni's multiple comparison	Group × time interaction	0.0053	F(1,45) = 8.577
	15-dB SNR, n = 22 cells from four mice			5-dB SNR Pre vs. During	<0.0001	
				15-dB SNR Pre vs. During	0.2156	
Fig. 2D (left)	mCherry, n = 10 mice	Mann-Whitney U test		mCherry vs. hM4Di-mCherry at BL	0.3816	U = 26.5
	hM4Di-mCherry, n = 8 mice			mCherry vs. hM4Di-mCherry at CNO	<0.0001	U = 0
Fig. 2D (right)	mCherry, n = 9 mice	two-tailed unpaired Student's t-test		mCherry vs. hM4Di-mCherry	0.0006	t16 = 4.283
	hM4Di-mCherry, n = 9 mice					
Fig. 2E	mCherry, n = 10 mice	Two-way RM ANOVA	Bonferroni's multiple comparison	Group × time interaction	< 0.0001	F(1,18) = 27.29
	hM4Di-mCherry, n = 10 mice			mCherry vs. hM4Di-mCherry at BL	>0.9999	
				mCherry vs. hM4Di-mCherry at CNO	<0.0001	
Fig. 2N	n = 12 cells from four mice	two-tailed paired Student's t-test		ACSF vs. DNQX	0.0002	t11 = 5.337
Fig. 2O	n = 14 cells from four mice	two-tailed paired Student's t-test		ACSF vs. DNQX	0.0001	t13 = 6.634
Fig. 3B	n = 19 cells from four mice	two-tailed paired Student's t-test		BL vs. STS	0.5079	t18 = 0.6756
Fig. 3C	n = 27 cells from five mice	two-tailed paired Student's t-test		BL vs. STS	0.0003	t26 = 4.213
Fig. 3E	Control, n = 24 cells from four mice	Two-way RM ANOVA	Bonferroni's multiple comparison	Group × time interaction	< 0.0001	F(1,69) = 19.67
	5-dB SNR, n = 47 cells from eight mice			Control Pre vs. During	>0.9999	
				5-dB SNR Pre vs. During	<0.0001	
Fig. 3F	n = 71 cells from seven mice	two-tailed paired Student's t-test		Pre-light × Light on	< 0.0001	t70 = 0.6756
Fig. 3H	EYFP, n = 10 mice	Two-way RM ANOVA	Bonferroni's multiple comparison	Group × time interaction	< 0.0001	F(2,34) = 103.9
	eNpHR3.0-EYFP, n = 9 mice			EYFP Pre vs. Light	0.6105	
				eNpHR3.0-EYFP Pre vs. Light	<0.0001	
Fig. 3I	EYFP, n = 8 mice	Two-way RM ANOVA	Bonferroni's multiple comparison	Group × time interaction	< 0.0001	F(2,30) = 20.05
	eNpHR3.0-EYFP, n = 9 mice			EYFP Pre vs. Light	0.2888	
				eNpHR3.0-EYFP Pre vs. Light	0.0016	
Fig. 3J	EYFP, n = 10 mice	two-tailed unpaired Student's t-test		EYFP vs. eNpHR3.0-EYFP	0.0001	t18 = 4.849
	eNpHR3.0-EYFP, n = 10 mice					
Fig. 3N	5-dB SNR, n = 20 cells from four mice	Two-way RM ANOVA	Bonferroni's multiple comparison	Group × time interaction	< 0.0001	F(1,33) = 41.31
	15-dB SNR, n = 15 cells from four mice			5-dB SNR Pre vs. During	<0.0001	
				15-dB SNR Pre vs. During	0.0683	
Fig. 4B	n = 36 cells from four mice	two-tailed paired Student's t-test		BL vs. STS	0.089	t35 = 1.749
Fig. 4C	BL, n = 18 cells from four mice	two-tailed paired Student's t-test		BL vs. STS	< 0.0001	t17 = 7.373
Fig. 4E	Control, n = 21 cells from four mice	Two-way RM ANOVA	Bonferroni's multiple comparison	Group vs. time interaction	< 0.0001	F(1,42) = 24.18
	5-dB SNR, n = 23 cells from four mice			Control Pre vs. During	>0.9999	
				5-dB SNR Pre vs. During	<0.0001	
Fig. 4G	n = 67 cells from seven mice	two-tailed paired Student's t-test		Pre-light vs. Light on	< 0.0001	t66 = 12.14
Fig. 4H	EYFP, n = 10 mice	Two-way RM ANOVA	Bonferroni's multiple comparison	Group vs. time interaction	< 0.0001	F(2,34) = 20.98
	eNpHR3.0-EYFP = 9 mice			EYFP Pre vs. Light	>0.9999	
				eNpHR3.0-EYFP Pre vs. Light	0.0005	
Fig. 4I	EYFP, n = 10 mice	Two-way RM ANOVA	Bonferroni's multiple comparison	Group × time interaction	< 0.0001	F(2,34) = 13.25
	eNpHR3.0-EYFP, n = 9 mice			EYFP Pre vs. Light	0.2888	
				eNpHR3.0-EYFP Pre vs. Light	0.0016	
Fig. 4J	EYFP, n = 10	two-tailed unpaired Student's t-test		EYFP vs. eNpHR3.0-EYFP	< 0.0001	t17 = 5.648
	eNpHR3.0-EYFP, n = 9					
Fig. 4M	5-dB SNR, n = 35 cells from four mice	Two-way RM ANOVA	Bonferroni's multiple comparison	Group × time interaction	< 0.0001	F(1,69) = 24.24
	15-dB SNR, n = 36 cells from four mice			5-dB SNR Pre vs. During	<0.0001	
				15-dB SNR Pre vs. During	0.1861	

Table S2. Extended statistical information for Figure S1 to Figure S24.

Figure Panel	n/group	Primary statistic	*Post-hoc* test	Comparison	p value	Statistic
Fig. S1A	Saline, n = 9 mice	Two-way RM ANOVA		Group × time interaction	<0.0001	F (3,51) = 9.696
	CFA, n = 10 mice					
Fig. S1B	50 dB SPL DS, n =10 mice	Two-way RM ANOVA		Group × time interaction	0.9129	F(4,52) = 0.2424
	50 dB SPL CS, n =10 mice					
	50 dB SPL WN, n = 9 mice					
Fig. S1C	35 dB SPL, n =8 mice	Two-way RM ANOVA	Bonferroni's multiple comparison	Group × time interaction	<0.0001	F(3,31) = 21.50
	40 dB SPL, n = 9 mice			35 dB SPL Pre vs. During	<0.0001	
	45 dB SPL, n = 8 mice			40 dB SPL Pre vs. During	0.0931	
	50 dB SPL, n = 10 mice			45 dB SPL Pre vs. During	>0.9999	
				50 dB SPL Pre vs. During	>0.9999	
Fig. S1D	Saline, n = 10	Two-way RM ANOVA		Group × time interaction	<0.0001	F(3,54) = 33.78
	CFA, n = 10					
Fig. S2A	Sham, n = 8	Two-way RM ANOVA		Group × time interaction	< 0.0001	F(3,45) = 12.25
	SNI, n = 9					
Fig. S2B	Ambient noise, n = 10	Two-way RM ANOVA	Bonferroni's multiple comparison	Group × time interaction	< 0.0001	F(18,250) = 14.72
	50 dB SPL CS, n = 10			Ambient noise vs. 50 dB at BL	0.9969	
	60 dB SPL CS, n = 8			Ambient noise vs. 50 dB at 10 min	<0.0001	
				Ambient noise vs. 50 dB at 20 min	<0.0001	
				Ambient noise vs. 50 dB at 30 min	<0.0001	
				Ambient noise vs. 50 dB at 40 min	0.5494	
				Ambient noise vs. 50 dB at 50 min	0.9521	
				Ambient noise vs. 50 dB at 24 H	0.9969	
				Ambient noise vs. 50 dB at 48 H	0.021	
				Ambient noise vs. 50 dB at 72 H	0.002	
				Ambient noise vs. 50 dB at 96 H	<0.0001	
				Ambient noise vs. 60 dB at BL	0.9796	
				Ambient noise vs. 60 dB at 10 min	0.9973	
				Ambient noise vs. 60 dB at 20 min	0.9341	
				Ambient noise vs. 60 dB at 30 min	0.9208	
				Ambient noise vs. 60 dB at 40 min	0.84	
				Ambient noise vs. 60 dB at 50 min	0.9403	
				Ambient noise vs. 60 dB at 24 H	0.9939	
				Ambient noise vs. 60 dB at 48 H	0.9917	
				Ambient noise vs. 60 dB at 72 H	0.9065	
				Ambient noise vs. 60 dB at 96 H	0.5704	
Fig. S2C	Ambient noise, n = 10	Two-way RM ANOVA	Bonferroni's multiple comparison	Group × time interaction	< 0.0001	F(18,230) = 12.6
	50 dB SPL DS, n = 8			Ambient noise vs. 50 dB at BL	0.9651	
	60 dB SPL DS, n = 8			Ambient noise vs. 50 dB at 10 min	<0.0001	
				Ambient noise vs. 50 dB at 20 min	<0.0001	
				Ambient noise vs. 50 dB at 30 min	<0.0001	
				Ambient noise vs. 50 dB at 40 min	0.4952	
				Ambient noise vs. 50 dB at 50 min	0.9702	
				Ambient noise vs. 50 dB at 24 H	0.9702	
				Ambient noise vs. 50 dB at 48 H	0.4311	
				Ambient noise vs. 50 dB at 72 H	0.0136	
				Ambient noise vs. 50 dB at 96 H	<0.0001	
				Ambient noise vs. 60 dB at BL	0.9898	
				Ambient noise vs. 60 dB at 10 min	0.9034	
				Ambient noise vs. 60 dB at 20 min	0.2155	
				Ambient noise vs. 60 dB at 30 min	0.7563	
				Ambient noise vs. 60 dB at 40 min	0.7678	
				Ambient noise vs. 60 dB at 50 min	0.7791	
				Ambient noise vs. 60 dB at 24 H	0.4086	
				Ambient noise vs. 60 dB at 48 H	0.6112	
				Ambient noise vs. 60 dB at 72 H	0.5558	
				Ambient noise vs. 60 dB at 96 H	0.9342	
Fig. S2D	Ambient noise, n = 10	Two-way RM ANOVA	Bonferroni's multiple comparison	Group × time interaction	< 0.0001	F(18,198) = 7.238
	50 dB SPL WN, n = 8			Ambient noise vs. 50 dB at BL	0.0703	
	60 dB SPL WN, n = 7			Ambient noise vs. 50 dB at 10 min	0.0031	
				Ambient noise vs. 50 dB at 20 min	0.0238	
				Ambient noise vs. 50 dB at 30 min	0.0268	
				Ambient noise vs. 50 dB at 40 min	>0.9999	
				Ambient noise vs. 50 dB at 50 min	>0.9999	
				Ambient noise vs. 50 dB at 24 H	>0.9999	
				Ambient noise vs. 50 dB at 48 H	0.0005	
				Ambient noise vs. 50 dB at 72 H	0.0381	
				Ambient noise vs. 50 dB at 96 H	0.029	
				Ambient noise vs. 60 dB at BL	>0.9999	
				Ambient noise vs. 60 dB at 10 min	>0.9999	
				Ambient noise vs. 60 dB at 20 min	>0.9999	
				Ambient noise vs. 60 dB at 30 min	>0.9999	
				Ambient noise vs. 60 dB at 40 min	>0.9999	
				Ambient noise vs. 60 dB at 50 min	>0.9999	
				Ambient noise vs. 60 dB at 24 H	>0.9999	
				Ambient noise vs. 60 dB at 48 H	>0.9999	
				Ambient noise vs. 60 dB at 72 H	0.7734	

Table S2. Extended statistical information for Figure S1 to Figure S24.

Figure Panel	n/group	Primary statistic	*Post-hoc* test	Comparison	p value	Statistic
				Ambient noise vs. 60 dB at 96 H	>0.9999	
Fig. S2E	35 dB SPL, n = 10	Two-way RM ANOVA	Bonferroni's multiple comparison	Group × time interaction	< 0.0001	F(3,36) = 39.96
	40 dB SPL, n = 10			35 dB SPL Pre vs. During	<0.0001	
	45 dB SPL, n = 10			40 dB SPL Pre vs. During	0.0931	
	50 dB SPL, n = 10			45 dB SPL Pre vs. During	>0.9999	
				50 dB SPL Pre vs. During	>0.9999	
Fig. S2F	62 dB SPL, n = 8	Two-way RM ANOVA	Bonferroni's multiple comparison	Group × time interaction	< 0.0001	F(3,32) = 27.10
	67 dB SPL, n = 10			62 dB SPL Pre vs. During	<0.0001	
	72 dB SPL, n = 8			67 dB SPL Pre vs. During	0.0526	
	77 dB SPL, n = 10			72 dB SPL Pre vs. During	>0.9999	
				77 dB SPL Pre vs. During	>0.9999	
Fig. S2G	Sham, n = 10	Two-way RM ANOVA		Group × time interaction	< 0.0001	F(3,54) = 16.44
	SNI, n = 10					
Fig. S2H	Ambient noise, n = 10	Two-way RM ANOVA	Bonferroni's multiple comparison	Group × time interaction	< 0.0001	F(18,243) = 5.043
	5-dB SNR, n = 10			Ambient noise vs. 5-dB SNR at BL	0.6196	
	15-dB SNR, n = 10			Ambient noise vs. 5-dB SNR at 10 min	0.0004	
				Ambient noise vs. 5-dB SNR at 20 min	<0.0001	
				Ambient noise vs. 5-dB SNR at 30 min	0.0002	
				Ambient noise vs. 5-dB SNR at 40 min	0.4479	
				Ambient noise vs. 5-dB SNR at 50 min	>0.9999	
				Ambient noise vs. 5-dB SNR at 24 H	>0.9999	
				Ambient noise vs. 5-dB SNR at 48 H	0.0005	
				Ambient noise vs. 5-dB SNR at 72 H	0.0036	
				Ambient noise vs. 5-dB SNR at 96 H	0.0001	
				Ambient noise vs. 15-dB SNR at BL	0.0613	
				Ambient noise vs. 15-dB SNR at 10 min	0.5023	
				Ambient noise vs. 15-dB SNR at 20 min	0.5071	
				Ambient noise vs. 15-dB SNR at 30 min	0.52	
				Ambient noise vs. 15-dB SNR at 40 min	0.1508	
				Ambient noise vs. 15-dB SNR at 50 min	0.6707	
				Ambient noise vs. 15-dB SNR at 24 H	0.6839	
				Ambient noise vs. 15-dB SNR at 48 H	0.8289	
				Ambient noise vs. 15-dB SNR at 72 H	>0.9999	
				Ambient noise vs. 15-dB SNR at 96 H	>0.9999	
Fig. S3A	Saline, n = 10	Two-way RM ANOVA		Group × time interaction	< 0.0001	F(8,144) = 21.90
	Capsaicin, n = 10					
Fig. S3B	Saline, n = 10	Two-way RM ANOVA		Group × time interaction	< 0.0001	F(8,144) = 18.94
	Capsaicin, n = 10					
Fig. S3C	Ambient noise, n = 10	Wilcoxon matched-paired signed rank test		Ambient noise Pre vs. During	0.5	W = 3
	5-dB SNR, n = 10			5-dB SNR Pre vs. During	0.002	W = 55
	15-dB SNR, n = 10			15-dB SNR Pre vs. During	>0.9999	W = -2
Fig. S3D	Ambient noise, n = 10	Two-way RM ANOVA	Bonferroni's multiple comparison	Group × time interaction	0.0005	F(2,27) = 10.21
	5-dB SNR, n = 10			Ambient noise Pre vs. During	>0.9999	
	15-dB SNR, n = 10			5-dB SNR Pre vs. During	<0.0001	
				15-dB SNR Pre vs. During	>0.9999	
Fig. S4A	Ambient noise, n = 10	Two-way RM ANOVA	Bonferroni's multiple comparison	Group × time interaction	0.0007	F(18,243) = 2.553
	5-dB SNR, n = 10			Ambient noise vs. 5-dB SNR at BL	>0.9999	
	15-dB SNR, n = 10			Ambient noise vs. 5-dB SNR at 10 min	0.0315	
				Ambient noise vs. 5-dB SNR at 20 min	0.0318	
				Ambient noise vs. 5-dB SNR at 30 min	0.0204	
				Ambient noise vs. 5-dB SNR at 40 min	0.0767	
				Ambient noise vs. 5-dB SNR at 50 min	0.096	
				Ambient noise vs. 5-dB SNR at 24 H	0.3249	
				Ambient noise vs. 5-dB SNR at 48 H	0.0423	
				Ambient noise vs. 5-dB SNR at 72 H	0.0494	
				Ambient noise vs. 5-dB SNR at 96 H	0.0246	
				Ambient noise vs. 15-dB SNR at BL	0.0884	
				Ambient noise vs. 15-dB SNR at 10 min	0.1244	
				Ambient noise vs. 15-dB SNR at 20 min	0.0168	
				Ambient noise vs. 15-dB SNR at 30 min	0.4633	
				Ambient noise vs. 15-dB SNR at 40 min	0.0021	
				Ambient noise vs. 15-dB SNR at 50 min	0.5041	
				Ambient noise vs. 15-dB SNR at 24 H	>0.9999	
				Ambient noise vs. 15-dB SNR at 48 H	>0.9999	
				Ambient noise vs. 15-dB SNR at 72 H	>0.9999	
				Ambient noise vs. 15-dB SNR at 96 H	>0.9999	
Fig. S4B	Ambient noise, n = 10	Two-way RM ANOVA	Bonferroni's multiple comparison	Group × time interaction	0.0004	F(18,243) = 2.639
	5-dB SNR, n = 10			Ambient noise vs. 5-dB SNR at BL	>0.9999	
	15-dB SNR, n = 10			Ambient noise vs. 5-dB SNR at 10 min	0.0056	
				Ambient noise vs. 5-dB SNR at 20 min	<0.0001	
				Ambient noise vs. 5-dB SNR at 30 min	0.015	
				Ambient noise vs. 5-dB SNR at 40 min	>0.9999	
				Ambient noise vs. 5-dB SNR at 50 min	>0.9999	
				Ambient noise vs. 5-dB SNR at 24 H	>0.9999	
				Ambient noise vs. 5-dB SNR at 48 H	0.0019	

Table S2. Extended statistical information for Figure S1 to Figure S24.

Figure Panel	n/group	Primary statistic	*Post-hoc* test	Comparison	p value	Statistic
				Ambient noise vs. 5-dB SNR at 72 H	0.0436	
				Ambient noise vs. 5-dB SNR at 96 H	0.1697	
				Ambient noise vs. 15-dB SNR at BL	0.7654	
				Ambient noise vs. 15-dB SNR at 10 min	>0.9999	
				Ambient noise vs. 15-dB SNR at 20 min	>0.9999	
				Ambient noise vs. 15-dB SNR at 30 min	>0.9999	
				Ambient noise vs. 15-dB SNR at 40 min	0.0933	
				Ambient noise vs. 15-dB SNR at 50 min	0.0825	
				Ambient noise vs. 15-dB SNR at 24 H	>0.9999	
				Ambient noise vs. 15-dB SNR at 48 H	0.8839	
				Ambient noise vs. 15-dB SNR at 72 H	>0.9999	
				Ambient noise vs. 15-dB SNR at 96 H	>0.9999	
Fig. S4C	Ambient noise, n = 10 5-dB SNR, n = 10 15-dB SNR, n = 10	Two-way RM ANOVA	Bonferroni's multiple comparison	Group × time interaction	< 0.0001	F(18,243) = 6.572
				Ambient noise vs. 5-dB SNR at BL	>0.9999	
				Ambient noise vs. 5-dB SNR at 10 min	0.0156	
				Ambient noise vs. 5-dB SNR at 20 min	0.0177	
				Ambient noise vs. 5-dB SNR at 30 min	<0.0001	
				Ambient noise vs. 5-dB SNR at 40 min	0.0054	
				Ambient noise vs. 5-dB SNR at 50 min	0.073	
				Ambient noise vs. 5-dB SNR at 24 H	<0.0001	
				Ambient noise vs. 5-dB SNR at 48 H	0.0023	
				Ambient noise vs. 5-dB SNR at 72 H	0.0006	
				Ambient noise vs. 5-dB SNR at 96 H	0.0011	
				Ambient noise vs. 15-dB SNR at BL	0.4144	
				Ambient noise vs. 15-dB SNR at 10 min	0.5036	
				Ambient noise vs. 15-dB SNR at 20 min	0.5803	
				Ambient noise vs. 15-dB SNR at 30 min	0.5803	
				Ambient noise vs. 15-dB SNR at 40 min	0.2434	
				Ambient noise vs. 15-dB SNR at 50 min	0.3117	
				Ambient noise vs. 15-dB SNR at 24 H	0.2872	
				Ambient noise vs. 15-dB SNR at 48 H	>0.9999	
				Ambient noise vs. 15-dB SNR at 72 H	>0.9999	
				Ambient noise vs. 15-dB SNR at 96 H	>0.9999	
Fig. S4D	Ambient noise, n = 10 5-dB SNR, n = 9 15-dB SNR, n = 10	Two-way RM ANOVA	Bonferroni's multiple comparison	Group × time interaction	< 0.0001	F(18,225) = 17.99
				Ambient noise vs. 5-dB SNR at BL	>0.9999	
				Ambient noise vs. 5-dB SNR at 10 min	0.0001	
				Ambient noise vs. 5-dB SNR at 20 min	<0.0001	
				Ambient noise vs. 5-dB SNR at 30 min	<0.0001	
				Ambient noise vs. 5-dB SNR at 40 min	>0.9999	
				Ambient noise vs. 5-dB SNR at 50 min	>0.9999	
				Ambient noise vs. 5-dB SNR at 24 H	<0.0001	
				Ambient noise vs. 5-dB SNR at 48 H	<0.0001	
				Ambient noise vs. 5-dB SNR at 72 H	<0.0001	
				Ambient noise vs. 5-dB SNR at 96 H	<0.0001	
				Ambient noise vs. 15-dB SNR at BL	>0.9999	
				Ambient noise vs. 15-dB SNR at 10 min	>0.9999	
				Ambient noise vs. 15-dB SNR at 20 min	>0.9999	
				Ambient noise vs. 15-dB SNR at 30 min	0.6951	
				Ambient noise vs. 15-dB SNR at 40 min	>0.9999	
				Ambient noise vs. 15-dB SNR at 50 min	>0.9999	
				Ambient noise vs. 15-dB SNR at 24 H	>0.9999	
				Ambient noise vs. 15-dB SNR at 48 H	>0.9999	
				Ambient noise vs. 15-dB SNR at 72 H	>0.9999	
				Ambient noise vs. 15-dB SNR at 96 H	>0.9999	
Fig. S4E	Ambient noise, n = 10 5-dB SNR, n = 10 15-dB SNR, n = 10	Wilcoxon matched-paired signed rank test		Ambient noise Pre vs. During	0.75	W = -2
				5-dB SNR Pre vs. During	0.002	W = 55
				15-dB SNR Pre vs. During	>0.9999	W = 1
Fig. S4F	Ambient noise, n = 10 5-dB SNR, n = 10 15-dB SNR, n = 10	Two-way RM ANOVA	Bonferroni's multiple comparison	Group × time interaction	< 0.0001	F(2,27) = 16.97
				Ambient noise Pre vs. During	0.9453	
				5-dB SNR Pre vs. During	<0.0001	
				5-dB SNR Pre vs. During	0.9655	
Fig. S5A	Saline, n = 10 CFA, n = 9	two-tailed unpaired Student's *t* -test		Saline vs. CFA	0.005	t17 = 3.22
Fig. S5C	Sham + Ambient noise, n = 9 SNI + Ambient noise, n = 10 SNI + 50 dB SPL WN, n = 8 SNI + 60 dB SPL WN, n = 9	One-way ANOVA	Bonferroni's multiple comparison	Main effect of group	< 0.0001	F(3,32) = 10.92
				Sham + Ambient noise vs. SNI + Ambient noise	0.0123	
				SNI + Ambient noise vs. SNI + 5-dB SNR WN	< 0.0001	
				SNI + Ambient noise vs. SNI+ 15-dB SNR WN	0.1634	
Fig. S5D	Ambient noise, n = 9 5-dB SNR, n = 9 15-dB SNR, n = 8	One-way ANOVA	Bonferroni's multiple comparison	Main effect of group	0.019	F(2,23) = 4.732
				Ambient noise vs. 5-dB SNR	0.0253	
				Ambient noise vs. 15-dB SNR	0.0847	
Fig. S6B	CFA Ambient noise, n = 10 CFA 5-dB SNR, n = 10 CFA 15-dB SNR, n = 10	One-way ANOVA	Bonferroni's multiple comparison	Main effect of group	0.6999	F(2,27) = 0.3616
				Ambient noise vs. 5-dB SNR	>0.9999	
				Ambient noise vs. 15-dB SNR	>0.9999	
	SNI Ambient noise, n = 9 SNI 5-dB SNR, n = 9	One-way ANOVA	Bonferroni's multiple comparison	Main effect of group	0.9072	F(2,24) = 0.0978
				Ambient noise vs. 5-dB SNR	>0.9999	

Table S2. Extended statistical information for Figure S1 to Figure S24.

Figure Panel	n/group	Primary statistic	*Post-hoc* test	Comparison	p value	Statistic
	SNI 15-dB SNR, n = 9			Ambient noise vs. 15-dB SNR	>0.9999	
Fig. S6D	CFA Ambient noise, n = 10	One-way ANOVA	Bonferroni's multiple comparison	Main effect of group	0.1757	F(2,27) = 1.856
	CFA 5-dB SNR, n = 10			Ambient noise vs. 5-dB SNR	0.6711	
	CFA 15-dB SNR, n = 10			Ambient noise vs. 15-dB SNR	>0.9999	
	SNI Ambient noise, n = 10	One-way ANOVA	Bonferroni's multiple comparison	Main effect of group	0.961	F (2,26) = 0.03989
	SNI 5-dB SNR, n = 10			Ambient noise vs. 5-dB SNR	>0.9999	
	SNI 15-dB SNR, n = 9			Ambient noise vs. 15-dB SNR	>0.9999	
Fig. S6F	CFA Ambient noise, n = 10	One-way ANOVA	Bonferroni's multiple comparison	Main effect of group	0.885	F(2,27) = 0.1227
	CFA 5-dB SNR, n = 10			Ambient noise vs. 5-dB SNR	>0.9999	
	CFA 15-dB SNR, n = 10			Ambient noise vs. 15-dB SNR	>0.9999	
	SNI Ambient noise, n = 10	One-way ANOVA	Bonferroni's multiple comparison	Main effect of group	0.7413	F(2,27) = 0.3026
	SNI 5-dB SNR, n = 10			Ambient noise vs. 5-dB SNR	>0.9999	
	SNI 15-dB SNR, n = 10			Ambient noise vs. 15-dB SNR	>0.9999	
Fig. S6G	Saline, n = 9 mice	One-way ANOVA	Bonferroni's multiple comparison	Main effect of group	< 0.0001	F (3,32) = 11.12
	CFA 3W+Ambient noise, n = 9 mice			Saline vs. CFA 3W+Ambient noise	0.0004	
	CFA 3W+5-dB SNR, n = 9 mice			CFA 3W+Ambient noise vs. CFA 3W+5-dB SNR	>0.9999	
	CFA 3W+15-dB SNR, n = 9 mice			CFA 3W+Ambient noise vs. CFA 3W+15-dB SNR	>0.9999	
Fig. S6H	Saline, n = 9 mice	One-way ANOVA	Bonferroni's multiple comparison	Main effect of group	0.0056	F (3,33) = 5.026
	CFA 3W+Ambient noise, n = 10 mice			Saline vs. CFA 3W+Ambient noise	0.0139	
	CFA 3W+5-dB SNR, n = 9 mice			CFA 3W+Ambient noise vs. CFA 3W+5-dB SNR	>0.9999	
	CFA 3W+15-dB SNR, n = 9 mice			CFA 3W+Ambient noise vs. CFA 3W+15-dB SNR	>0.9999	
Fig. S6I	Saline, n = 9 mice	One-way ANOVA	Bonferroni's multiple comparison	Main effect of group	<0.0001	F (3,32) = 19.07
	CFA 3W+Ambient noise, n = 9 mice			Saline vs. CFA 3W+Ambient noise	<0.0001	
	CFA 3W+5-dB SNR, n = 9 mice			CFA 3W+Ambient noise vs. CFA 3W+5-dB SNR	>0.9999	
	CFA 3W+15-dB SNR, n = 9 mice			CFA 3W+Ambient noise vs. CFA 3W+15-dB SNR	>0.9999	
Fig. S6J	Sham, n = 10 mice	One-way ANOVA	Bonferroni's multiple comparison	Main effect of group	0.0001	F (3,31) = 9.507
	SNI 6W+Ambient noise, n = 9 mice			Sham vs. SNI 6W+Ambient noise	0.0024	
	SNI 6W+5-dB SNR, n = 8 mice			SNI 6W+Ambient noise vs. SNI 6W+5-dB SNR	>0.9999	
	SNI 6W+15-dB SNR, n = 8 mice			SNI 6W+Ambient noise vs. SNI 6W+15-dB SNR	>0.9999	
Fig. S6K	Sham, n = 10 mice	One-way ANOVA	Bonferroni's multiple comparison	Main effect of group	<0.0001	F (3,31) = 15.47
	SNI 6W+Ambient noise, n = 9 mice			Sham vs. SNI 6W+Ambient noise	<0.0001	
	SNI 6W+5-dB SNR, n = 8 mice			SNI 6W+Ambient noise vs. SNI 6W+5-dB SNR	>0.9999	
	SNI 6W+15-dB SNR, n = 8 mice			SNI 6W+Ambient noise vs. SNI 6W+15-dB SNR	>0.9999	
Fig. S6L	Sham, n = 10 mice	One-way ANOVA	Bonferroni's multiple comparison	Main effect of group	<0.0001	F (3,32) = 16.64
	SNI 6W+Ambient noise, n = 10 mice			Sham vs. SNI 6W+Ambient noise	<0.0001	
	SNI 6W+5-dB SNR, n = 8 mice			SNI 6W+Ambient noise vs. SNI 6W+5-dB SNR	>0.9999	
	SNI 6W+15-dB SNR, n = 8 mice			SNI 6W+Ambient noise vs. SNI 6W+15-dB SNR	>0.9999	
Fig. S7A	Ambient noise, n = 5 mice	One-way ANOVA	Bonferroni's multiple comparison	Main effect of group	0.4785	F (2,12) = 0.7843
	5-dB SNR, n = 5 mice			Ambient noise vs. 5-dB SNR	0.6576	
	15-dB SNR, n = 5 mice			Ambient noise vs. 15-dB SNR	0.6546	
Fig. S7B	Ambient noise, n = 5 mice	One-way ANOVA	Bonferroni's multiple comparison	Main effect of group	0.9012	F (2,12) = 0.1050
	5-dB SNR, n = 5 mice			Ambient noise vs. 5-dB SNR	>0.9999	
	15-dB SNR, n = 5 mice			Ambient noise vs. 15-dB SNR	>0.9999	
Fig. S7C	Ambient noise, n = 5 mice	One-way ANOVA	Bonferroni's multiple comparison	Main effect of group	0.7602	F (2,12) = 0.2805
	5-dB SNR, n = 5 mice			Ambient noise vs. 5-dB SNR	>0.9999	
	15-dB SNR, n = 5 mice			Ambient noise vs. 15-dB SNR	>0.9999	
Fig. S8A	Vehicle, n = 9 mice	Mann-Whitney U test		Vehicle vs. Naloxone at BL	>0.9999	U = 39.5
	Naloxone, n = 9 mice			Vehicle vs. Naloxone at 5-dB SNR	0.9914	U = 38.5
Fig. S8B	Vehicle, n = 10 mice	Two-way RM ANOVA	Bonferroni's multiple comparison	Group × time interaction	0.8287	F (1,16) = 0.04835
	Naloxone, n = 9 mice			Vehicle vs. Naloxone at BL	>0.9999	
				Vehicle vs. Naloxone at 5-dB SNR	>0.9999	
Fig. S8C	Vehicle, n = 10 mice	Mann-Whitney U test		Vehicle vs. Naloxone at BL	0.9294	U = 36.5
	Naloxone, n = 10 mice			Vehicle vs. Naloxone at 5-dB SNR	0.6686	U = 35
Fig. S8D	Vehicle, n = 9 mice	Two-way RM ANOVA	Bonferroni's multiple comparison	Group × time interaction	0.475	F (1,17) = 0.5337
	Naloxone, n = 10 mice			Vehicle vs. Naloxone at BL	>0.9999	
				Vehicle vs. Naloxone at 5-dB SNR	0.4268	
Fig. S8E	Vehicle, n = 8 mice	Mann-Whitney U test		Vehicle vs. Naloxone at BL	>0.9999	U = 35
	Naloxone, n = 9 mice			Vehicle vs. Naloxone at 5-dB SNR	0.4552	U = 27
Fig. S8F	Vehicle, n = 10 mice	Two-way RM ANOVA	Bonferroni's multiple comparison	Group × time interaction	0.4158	F (1,16) = 0.6980
	Naloxone, n = 10 mice			Vehicle vs. Naloxone at BL	0.9488	
				Vehicle vs. Naloxone at 5-dB SNR	>0.9999	
Fig. S11C	mCherry, n = 8	Two-way RM ANOVA	Bonferroni's multiple comparison	Group × time interaction	0.0011	F(2,28) = 8.849
	ChR2-mCherry, n = 8			mCherry vs. ChR2-mCherry at light	0.0166	
Fig. S11D	mCherry, n = 10 mice	Two-way RM ANOVA	Bonferroni's multiple comparison	Group × time interaction	< 0.0001	F(2,36) = 102.2
	ChR2-mCherry, n = 10 mice			mCherry vs. ChR2-mCherry at light	<0.0001	
Fig. S11E	mCherry, n = 9 mice	two-tailed unpaired Student's *t* -test		mCherry vs. ChR2-mCherry	0.0043	t16 = 3.323
	ChR2-mCherry, n = 9 mice					
Fig. S13F	Saline, n = 26 cells from four mice	two-tailed unpaired Student's *t* -test		Saline vs. CFA	0.0004	t53 = 3.771
	CFA, n = 29 cells from four mice					
Fig. S13G	n = 23 cells from four mice	two-tailed paired Student's t-test		Pre vs. 15-dB SNR	0.9725	t22 = 0.03488
Fig. S13I	n = 22 cells from four mice	two-tailed paired Student's t-test		Pre-light vs. Light on	0.9832	t21 = 0.02134
Fig. S13J	EYFP, n = 10	two-tailed unpaired Student's *t* -test		EYFP vs. eNpHR3.0-EYFP	0.0058	t17 = 3.151
	eNpHR3.0-EYFP, n = 9					
Fig. S14B (CPA)	EYFP, n = 10 mice	two-tailed unpaired Student's *t* -test		EYFP vs. eNpHR3.0-EYFP	0.0112	t18 = 2.825

Table S2. Extended statistical information for Figure S1 to Figure S24.

Figure Panel	n/group	Primary statistic	*Post-hoc* test	Comparison	p value	Statistic
	eNpHR3.0-EYFP, n = 10 mice					
Fig. S14B (CPP)	EYFP, n = 10 mice	two-tailed unpaired Student's *t* -test		EYFP vs. eNpHR3.0-EYFP	0.0052	t18 = 3.179
	eNpHR3.0-EYFP, n = 10 mice					
Fig. S14C	EYFP, n = 10 mice	Two-way RM ANOVA	Bonferroni's multiple comparison	Group × time interaction	< 0.0001	F (2,36) = 41.26
	eNpHR3.0-EYFP, n = 10 mice			EYFP Pre vs. During	>0.9999	
				eNpHR3.0-EYFP Pre vs. During	0.0002	
Fig. S14D	EYFP, n = 10 mice	Two-way RM ANOVA	Bonferroni's multiple comparison	Group × time interaction	< 0.0001	F (2,36) = 42.57
	eNpHR3.0-EYFP, n = 10 mice			EYFP Pre vs. Light	>0.9999	
				eNpHR3.0-EYFP Pre vs. Light	<0.0001	
Fig. S15B	mCherry, n = 9	Two-way RM ANOVA	Bonferroni's multiple comparison	Group × time interaction	0.0002	F(1,17) = 21.80
	ChR2-mCherry, n = 10			mCherry vs. ChR2-mCherry at 5-dB SNR 15 min	>0.9999	
				mCherry vs. ChR2-mCherry at BL	< 0.0001	
Fig. S15C	mCherry, n = 9	two-tailed unpaired Student's t-test		mCherry vs. ChR2-mCherry	< 0.0001	t16 = 6.971
	ChR2-mCherry, n = 9					
Fig. S15F	n = 70 cells from seven mice	two-tailed paired Student's t-test		Pre-light vs. Light on	< 0.0001	t69 = 7.072
Fig. S16C	5-dB SNR, n = 24 cells from four mice	Two-way RM ANOVA	Bonferroni's multiple comparison	Group × time interaction	0.0002	F(1,47) = 15.90
	15-dB SNR, n = 25 cells from four mice			5-dB SNR, Pre vs. During	< 0.0001	
				15-dB SNR, Pre vs. During	0.1383	
Fig. S16F	Saline, n = 21 cells from four mice	two-tailed unpaired Student's t-test		Saline vs. CFA	< 0.0001	t42 = 11.98
	CFA, n = 23 cells from four mice					
Fig. S16H (left)	mCherry, n = 8	Wilcoxon test		mCherry BL vs. CNO	>0.9999	W = 1
	hM4Di-mCherry, n = 8			hM4Di-mCherry BL vs. CNO	0.0078	W = 36
Fig. S16H (right)	mCherry, n = 8	two-tailed unpaired Student's t-test		mCherry vs. hM4Di-mCherry	0.0029	t14 = 3.601
	hM4Di-mCherry, n = 8					
Fig. S16I (left)	mCherry, n = 9	Two-way RM ANOVA	Bonferroni's multiple comparison	Group × time interaction	0.0017	F(1,15) = 14.47
	hM3Dq-mCherry, n = 8			hM4Di-mCherry vs. mCherry at BL	0.8625	
				hM4Di-mCherry vs. mCherry at 5-dB SNR 15 min	0.0002	
Fig. S16I (right)	mCherry, n = 10	two-tailed unpaired Student's t-test		mCherry vs. hM3Dq-mCherry	0.0072	t17 = 3.056
	hM3Dq-mCherry, n = 9					
Fig. S17B	Saline, n = 9	Two-way RM ANOVA		Group × time interaction	< 0.0001	F(3,48) = 30.28
	CFA, n = 9					
Fig. S17C	Ambient noise, n = 10	One-way ANOVA	Bonferroni's multiple comparison	Main effect of group	< 0.0001	F(2,26) = 27.04
	5-dB SNR, n = 10			Ambient noise vs. 5-dB SNR	<0.0001	
	15-dB SNR, n = 9			Ambient noise vs. 15-dB SNR	>0.9999	
Fig. S17D	Ambient noise, n = 10	One-way ANOVA	Bonferroni's multiple comparison	Main effect of group	< 0.0001	F(2,25) = 14.49
	5-dB SNR, n = 10			Ambient noise vs. 5-dB SNR	0.0002	
	15-dB SNR, n = 8			Ambient noise vs. 15-dB SNR	>0.9999	
Fig. S17E	Ambient noise, n = 10	One-way ANOVA	Bonferroni's multiple comparison	Main effect of group	0.0063	F(2,26) = 6.197
	5-dB SNR, n = 10			Ambient noise vs. 5-dB SNR	0.0106	
	15-dB SNR, n = 9			Ambient noise vs. 15-dB SNR	>0.9999	
Fig. S17J	Saline, n = 20 cells from three mice	two-tailed unpaired Student's t-test		Saline vs. CFA	0.0051	t36 = 2.98
	CFA, n = 18 cells from three mice					
Fig. S17K	n = 21 cells from three mice	two-tailed paired Student's t-test		Pre vs. During	0.0538	t20 = 2.049
Fig. S17M	EYFP, n = 10	two-tailed unpaired Student's t-test		EYFP vs. eNpHR3.0-EYFP	0.0155	t17 = 2.689
	eNpHR3.0-EYFP, n = 9					
Fig. S18B (CPA)	EYFP, n = 10 mice	two-tailed unpaired Student's *t* -test		EYFP vs. eNpHR3.0-EYFP	0.0124	t18 = 2.778
	eNpHR3.0-EYFP, n = 10 mice					
Fig. S18B (CPP)	EYFP, n = 9 mice	two-tailed unpaired Student's *t* -test		EYFP vs. eNpHR3.0-EYFP	0.0141	t17 = 2.736
	eNpHR3.0-EYFP, n = 10 mice					
Fig. S18C	EYFP, n = 10 mice	Two-way RM ANOVA	Bonferroni's multiple comparison	Group × time interaction	< 0.0001	F (2,32) = 23.58
	eNpHR3.0-EYFP, n = 8 mice			EYFP Pre vs. During	>0.9999	
				eNpHR3.0-EYFP Pre vs. During	0.0042	
Fig. S18D	EYFP, n = 10 mice	Two-way RM ANOVA	Bonferroni's multiple comparison	Group × time interaction	< 0.0001	F (2,36) = 76.64
	eNpHR3.0-EYFP, n = 10 mice			EYFP Pre vs. During	>0.9999	
				eNpHR3.0-EYFP Pre vs. During	<0.0001	
Fig. S19B	mCherry, n = 9	Two-way RM ANOVA	Bonferroni's multiple comparison	Group × time interaction	0.0073	F(1,17) = 9.291
	ChR2-mCherry, n = 10			mCherry vs. ChR2-mCherry at BL	>0.9999	
				mCherry vs. ChR2-mCherry at 5-dB SNR	<0.0001	
Fig. S19C	mCherry, n = 10	two-tailed unpaired Student's t-test		mCherry vs. ChR2-mCherry	0.0054	t15 = 3.246
	ChR2-mCherry, n = 7					
Fig. S19F	n = 72 cells from seven mice	two-tailed paired Student's t-test		Pre-light vs. Light on	< 0.0001	t71 = 7.759
Fig. S20D	5-dB SNR, n = 43 cells from five mice	Two-way RM ANOVA	Bonferroni's multiple comparison	Group × time interaction	< 0.0001	F(1,77) = 25.17
	15-dB SNR, n = 36 cells from five mice			15-dB SNR, Pre vs. During	0.2518	
				5-dB SNR, Pre vs. During	< 0.0001	
Fig. S20F	Saline, n = 37 cells from five mice	two-tailed unpaired Student's *t* -test		Saline vs. CFA	< 0.0001	t72 = 2.739
	CFA, n = 37 cells from five mice					
Fig. S20H	mCherry, n = 10	Mann-Whitney U test		mCherry vs. hM4Di-mCherry at BL	0.8208	U = 47
	hM4Di-mCherry, n = 10			mCherry vs. hM4Di-mCherry at CNO	<0.0001	U = 0
Fig. S20I	mCherry, n = 8	Mann-Whitney U test		mCherry vs. hM3Dq-mCherry at BL	0.393	U = 24.5
	hM3Dq-mCherry, n = 8			mCherry vs. hM3Dq-mCherry at CNO	0.0006	U = 2
Fig. S21B	mCherry, n = 9	Two-way RM ANOVA	Bonferroni's multiple comparison	Group × time interaction	0.795	F(2,34) = 0.231
	ChR2-mCherry, n = 10			mCherry Pre vs.Light	>0.9999	
				ChR2-mCherry Pre vs.Light	>0.9999	
Fig. S21C	EYFP, n = 10	Two-way RM ANOVA	Bonferroni's multiple comparison	Group × time interaction	0.3925	F(2,34) = 0.9613
	eNpHR3.0-EYFP, n = 9			EYFP Pre vs. Light	0.8704	
				eNpHR3.0-EYFP Pre vs. Light	>0.9999	

Table S2. Extended statistical information for Figure S1 to Figure S24.

Figure Panel	n/group	Primary statistic	*Post-hoc* test	Comparison	p value	Statistic
Fig. S21E	mCherry, n = 8	Two-way RM ANOVA	Bonferroni's multiple comparison	Group × time interaction	0.9891	F(2,32) = 0.011
	ChR2-mCherry, n = 10			mCherry Pre vs.Light	>0.9999	
				ChR2-mCherry Pre vs.Light	>0.9999	
Fig. S21F	EYFP, n = 8	Two-way RM ANOVA	Bonferroni's multiple comparison	Group × time interaction	0.7314	F(2,30) = 0.316
	eNpHR3.0-EYFP, n = 9			EYFP Pre vs. Light	>0.9999	
				eNpHR3.0-EYFP Pre vs. Light	>0.9999	
Fig. S22B	mCherry, n = 10	Two-way RM ANOVA	Bonferroni's multiple comparison	Group × time interaction	0.9077	F(1,18) = 0.01384
	hM4Di-mCherry, n = 10			mCherry vs. hM4Di-mCherry at BL	>0.9999	
				mCherry vs. hM4Di-mCherry at CNO	>0.9999	
Fig. S22C	mCherry, n = 8	Two-way RM ANOVA	Bonferroni's multiple comparison	Group × time interaction	0.4318	F(1,16) = 0.6504
	hM3Dq-mCherry, n = 10			mCherry vs. hM3Dq-mCherry at BL	>0.9999	
				mCherry vs. hM3Dq-mCherry at CNO	>0.9999	
Fig. S22E	mCherry, n = 8	Mann-Whitney U test		mCherry vs. hM4Di-mCherry at BL	0.4667	U = 24
	hM4Di-mCherry, n = 8			mCherry vs. hM4Di-mCherry at CNO	> 0.9999	U = 32
Fig. S22F	mCherry, n = 7	Mann-Whitney U test		mCherry vs. hM3Dq-mCherry at BL	0.4615	U = 17.5
	hM3Dq-mCherry, n = 7			mCherry vs. hM3Dq-mCherry at CNO	0.7855	U = 22
Fig. S23C	mCherry, n = 9 mice	Two-way RM ANOVA	Bonferroni's multiple comparison	Group × time interaction	0.2295	F(2,32) = 0.7963
	ChR2-mCherry, n = 9 mice			mCherry vs. ChR2-mCherry at During	>0.9999	
Fig. S23D	mCherry, n = 9 mice	Two-way RM ANOVA	Bonferroni's multiple comparison	Group × time interaction	0.0578	F(2,32) = 0.9439
	ChR2-mCherry, n = 9 mice			mCherry vs. ChR2-mCherry at During	>0.9999	
Fig. S23E	mCherry, n = 9 mice	Two-way RM ANOVA	Bonferroni's multiple comparison	Group × time interaction	0.1563	F(2,32) = 0.8559
	ChR2-mCherry, n = 9 mice			mCherry vs. ChR2-mCherry at During	>0.9999	
Fig. S23F	mCherry, n = 9 mice	Two-way RM ANOVA	Bonferroni's multiple comparison	Group × time interaction	0.4152	F(2,32) = 0.9037
	ChR2-mCherry, n = 9 mice			mCherry vs. ChR2-mCherry at During	>0.9999	
Fig. S23H	EYFP, n = 10 mice	Two-way RM ANOVA	Bonferroni's multiple comparison	Group × time interaction	0.8578	F(2,36) = 0.1541
	eNpHR3.0-EYFP, n = 10 mice			EYFP vs. eNpHR3.0-EYFP at During	>0.9999	
Fig. S23I	EYFP, n = 10 mice	Two-way RM ANOVA	Bonferroni's multiple comparison	Group × time interaction	0.9713	F(2,36) = 0.0292
	eNpHR3.0-EYFP, n = 10 mice			EYFP vs. eNpHR3.0-EYFP at During	>0.9999	
Fig. S23J	EYFP, n = 10 mice	Two-way RM ANOVA	Bonferroni's multiple comparison	Group × time interaction	0.6899	F(2,36) = 0.375
	eNpHR3.0-EYFP, n = 10 mice			EYFP vs. eNpHR3.0-EYFP at During	>0.9999	
Fig. S23K	EYFP, n = 10 mice	Two-way RM ANOVA	Bonferroni's multiple comparison	Group × time interaction	0.08698	F(2,36) = 0.9169
	eNpHR3.0-EYFP, n = 10 mice			EYFP vs. eNpHR3.0-EYFP at During	>0.9999	

References and Notes

1. W. J. Gardner, J. C. Licklider, A. Z. Weisz, Suppression of pain by sound. *Science* **132**, 32–33 (1960). doi:10.1126/science.132.3418.32 Medline

2. A. Keenan, J. K. Keithley, Integrative Review: Effects of Music on Cancer Pain in Adults. *Oncol. Nurs. Forum* **42**, E368–E375 (2015). doi:10.1188/15.ONF.E368-E375 Medline

3. T. N. Nguyen, S. Nilsson, A.-L. Hellström, A. Bengtson, Music therapy to reduce pain and anxiety in children with cancer undergoing lumbar puncture: A randomized clinical trial. *J. Pediatr. Oncol. Nurs.* **27**, 146–155 (2010). doi:10.1177/1043454209355983 Medline

4. L. Hartling, A. S. Newton, Y. Liang, H. Jou, K. Hewson, T. P. Klassen, S. Curtis, Music to reduce pain and distress in the pediatric emergency department: A randomized clinical trial. *JAMA Pediatr.* **167**, 826–835 (2013). doi:10.1001/jamapediatrics.2013.200 Medline

5. C. Boyd-Brewer, R. McCaffrey, Vibroacoustic sound therapy improves pain management and more. *Holist. Nurs. Pract.* **18**, 111–118 (2004). doi:10.1097/00004650-200405000-00002 Medline

6. M. P. Jensen, S. Hakimian, L. H. Sherlin, F. Fregni, New insights into neuromodulatory approaches for the treatment of pain. *J. Pain* **9**, 193–199 (2008). doi:10.1016/j.jpain.2007.11.003 Medline

7. E. A. Garza Villarreal, E. Brattico, L. Vase, L. Østergaard, P. Vuust, Superior analgesic effect of an active distraction versus pleasant unfamiliar sounds and music: The influence of emotion and cognitive style. *PLOS ONE* **7**, e29397 (2012). doi:10.1371/journal.pone.0029397 Medline

8. S. J. Lunde, P. Vuust, E. A. Garza-Villarreal, L. Vase, Music-induced analgesia: How does music relieve pain? *Pain* **160**, 989–993 (2019). doi:10.1097/j.pain.0000000000001452 Medline

9. C. E. Dobek, M. E. Beynon, R. L. Bosma, P. W. Stroman, Music modulation of pain perception and pain-related activity in the brain, brain stem, and spinal cord: A functional magnetic resonance imaging study. *J. Pain* **15**, 1057–1068 (2014). doi:10.1016/j.jpain.2014.07.006 Medline

10. M. E. Sachs, A. Habibi, A. Damasio, J. T. Kaplan, Dynamic intersubject neural synchronization reflects affective responses to sad music. *Neuroimage* **218**, 116512 (2020). doi:10.1016/j.neuroimage.2019.116512 Medline

11. C. Usui, E. Kirino, S. Tanaka, R. Inami, K. Nishioka, K. Hatta, T. Nakajima, K. Nishioka, R. Inoue, Music Intervention Reduces Persistent Fibromyalgia Pain and Alters Functional Connectivity Between the Insula and Default Mode Network. *Pain Med.* **21**, 1546–1552 (2020). doi:10.1093/pm/pnaa071 Medline

12. L. Bonetti, E. Brattico, F. Carlomagno, G. Donati, J. Cabral, N. T. Haumann, G. Deco, P. Vuust, M. L. Kringelbach, Rapid encoding of musical tones discovered in whole-brain connectivity. *Neuroimage* **245**, 118735 (2021). doi:10.1016/j.neuroimage.2021.118735 Medline

13. E. G. Jones, *The Thalamus* (Cambridge Univ. Press, ed. 2, 2007).

14. S. M. Sherman, R. W. Guillery, The role of the thalamus in the flow of information to the cortex. *Phil. Trans. R. Soc. Lond. B* **357**, 1695–1708 (2002). doi:10.1098/rstb.2002.1161 Medline

15. A. Mouraux, A. Diukova, M. C. Lee, R. G. Wise, G. D. Iannetti, A multisensory investigation of the functional significance of the "pain matrix". *Neuroimage* **54**, 2237–2249 (2011). doi:10.1016/j.neuroimage.2010.09.084 Medline

16. B. A. Vogt, D. L. Rosene, D. N. Pandya, Thalamic and cortical afferents differentiate anterior from posterior cingulate cortex in the monkey. *Science* **204**, 205–207 (1979). doi:10.1126/science.107587 Medline

17. A. N. Viaene, I. Petrof, S. M. Sherman, Properties of the thalamic projection from the posterior medial nucleus to primary and secondary somatosensory cortices in the mouse. *Proc. Natl. Acad. Sci. U.S.A.* **108**, 18156–18161 (2011). doi:10.1073/pnas.1114828108 Medline

18. K. S. Meda, T. Patel, J. M. Braz, R. Malik, M. L. Turner, H. Seifikar, A. I. Basbaum, V. S. Sohal, Microcircuit Mechanisms through which Mediodorsal Thalamic Input to Anterior Cingulate Cortex Exacerbates Pain-Related Aversion. *Neuron* **102**, 944–959.e3 (2019). doi:10.1016/j.neuron.2019.03.042 Medline

19. X. Zhu, H.-D. Tang, W.-Y. Dong, F. Kang, A. Liu, Y. Mao, W. Xie, X. Zhang, P. Cao, W. Zhou, H. Wang, Z. Farzinpour, W. Tao, X. Song, Y. Zhang, T. Xue, Y. Jin, J. Li, Z. Zhang, Distinct thalamocortical circuits underlie allodynia induced by tissue injury and by depression-like states. *Nat. Neurosci.* **24**, 542–553 (2021). doi:10.1038/s41593-021-00811-x Medline

20. G. Wagner, M. Koschke, T. Leuf, R. Schlösser, K.-J. Bär, Reduced heat pain thresholds after sad-mood induction are associated with changes in thalamic activity. *Neuropsychologia* **47**, 980–987 (2009). doi:10.1016/j.neuropsychologia.2008.10.021 Medline

21. X. R. Xiong, F. Liang, B. Zingg, X. Y. Ji, L. A. Ibrahim, H. W. Tao, L. I. Zhang, Auditory cortex controls sound-driven innate defense behaviour through corticofugal projections to inferior colliculus. *Nat. Commun.* **6**, 7224 (2015). doi:10.1038/ncomms8224 Medline

22. G. Gilam, J. J. Gross, T. D. Wager, F. J. Keefe, S. C. Mackey, What Is the Relationship between Pain and Emotion? Bridging Constructs and Communities. *Neuron* **107**, 17–21 (2020). doi:10.1016/j.neuron.2020.05.024 Medline

23. J. W. Grau, R. L. Hyson, S. F. Maier, J. Madden 4th, J. D. Barchas, Long-term stress-induced analgesia and activation of the opiate system. *Science* **213**, 1409–1411 (1981). doi:10.1126/science.7268445 Medline

24. S. Koelsch, Brain correlates of music-evoked emotions. *Nat. Rev. Neurosci.* **15**, 170–180 (2014). doi:10.1038/nrn3666 Medline

25. H. L. Read, J. A. Winer, C. E. Schreiner, Functional architecture of auditory cortex. *Curr. Opin. Neurobiol.* **12**, 433–440 (2002). doi:10.1016/S0959-4388(02)00342-2 Medline

26. J. A. Winer, in *The Mammalian Auditory Pathway: Neuroanatomy*, D. B. Webster, A. N. Popper, R. R. Fay, Eds. (Springer, 1992), pp. 222–409.

27. T. V. Salomons, G. D. Iannetti, M. Liang, J. N. Wood, The “Pain Matrix” in Pain-Free Individuals. *JAMA Neurol.* **73**, 755–756 (2016). doi:10.1001/jamaneurol.2016.0653 Medline

28. A. V. Apkarian, M. C. Bushnell, R. D. Treede, J. K. Zubieta, Human brain mechanisms of pain perception and regulation in health and disease. *Eur. J. Pain* **9**, 463–484 (2005). doi:10.1016/j.ejpain.2004.11.001 Medline

29. W. Zhou, Y. Jin, Q. Meng, X. Zhu, T. Bai, Y. Tian, Y. Mao, L. Wang, W. Xie, H. Zhong, N. Zhang, M.-H. Luo, W. Tao, H. Wang, J. Li, J. Li, B.-S. Qiu, J.-N. Zhou, X. Li, H. Xu, K. Wang, X. Zhang, Y. Liu, G. Richter-Levin, L. Xu, Z. Zhang, A neural circuit for comorbid depressive symptoms in chronic pain. *Nat. Neurosci.* **22**, 1649–1658 (2019). doi:10.1038/s41593-019-0468-2 Medline

30. D. D. Price, Central neural mechanisms that interrelate sensory and affective dimensions of pain. *Mol. Interv.* **2**, 392–403 (2002). doi:10.1124/mi.2.6.392 Medline

31. H. Head, G. Holmes, Sensory disturbances from cerebral lesions. *Brain* **34**, 102–254 (1911). doi:10.1093/brain/34.2-3.102

32. M. E. Diamond, M. Armstrong-James, M. J. Budway, F. F. Ebner, Somatic sensory responses in the rostral sector of the posterior group (POm) and in the ventral posterior medial nucleus (VPM) of the rat thalamus: Dependence on the barrel field cortex. *J. Comp. Neurol.* **319**, 66–84 (1992). doi:10.1002/cne.903190108 Medline

33. K. Wiech, M. Ploner, I. Tracey, Neurocognitive aspects of pain perception. *Trends Cogn. Sci.* **12**, 306–313 (2008). doi:10.1016/j.tics.2008.05.005 Medline

34. S. Leknes, I. Tracey, A common neurobiology for pain and pleasure. *Nat. Rev. Neurosci.* **9**, 314–320 (2008). doi:10.1038/nrn2333 Medline

35. W. Ren, M. V. Centeno, S. Berger, Y. Wu, X. Na, X. Liu, J. Kondapalli, A. V. Apkarian, M. Martina, D. J. Surmeier, The indirect pathway of the nucleus accumbens shell amplifies neuropathic pain. *Nat. Neurosci.* **19**, 220–222 (2016). doi:10.1038/nn.4199 Medline

36. M. L. Smith, N. Asada, R. C. Malenka, Anterior cingulate inputs to nucleus accumbens control the social transfer of pain and analgesia. *Science* **371**, 153–159 (2021). doi:10.1126/science.abe3040 Medline

37. V. N. Salimpoor, M. Benovoy, K. Larcher, A. Dagher, R. J. Zatorre, Anatomically distinct dopamine release during anticipation and experience of peak emotion to music. *Nat. Neurosci.* **14**, 257–262 (2011). doi:10.1038/nn.2726 Medline

38. M. N. Baliki, B. Petre, S. Torbey, K. M. Herrmann, L. Huang, T. J. Schnitzer, H. L. Fields, A. V. Apkarian, Corticostriatal functional connectivity predicts transition to chronic back pain. *Nat. Neurosci.* **15**, 1117–1119 (2012). doi:10.1038/nn.3153 Medline

39. S. Koelsch, T. Fritz, D. Y. v. Cramon, K. Müller, A. D. Friederici, Investigating emotion with music: An fMRI study. *Hum. Brain Mapp.* **27**, 239–250 (2006). doi:10.1002/hbm.20180 Medline

40. Y. Liu, A. Latremoliere, X. Li, Z. Zhang, M. Chen, X. Wang, C. Fang, J. Zhu, C. Alexandre, Z. Gao, B. Chen, X. Ding, J.-Y. Zhou, Y. Zhang, C. Chen, K. H. Wang, C. J. Woolf, Z. He, Touch and tactile neuropathic pain sensitivity are set by corticospinal projections. *Nature* **561**, 547–550 (2018). doi:10.1038/s41586-018-0515-2 Medline